WILEY

EcoEnergy

REVIEW OPEN ACCESS

Entropy-Driven Design of Stable High-Performance Sodium-Ion Battery Cathodes

Feng Zhan[1] | Chuzhang Hong[1] | Yue Luo[2,3] | Jinhua Sun[4] | Hua Fan[5] | Zhiming Feng[6] | Jie Yang[7] | Xinhua Liu[8] | Rui Tan[2,3]

[1]School of Resources, Environment and Materials, Guangxi University, Nanning, China | [2]Department of Chemical Engineering, Swansea University, Swansea, UK | [3]Circular Approaches to Utilise and Retain Energy (CAPTURE), Swansea University, Swansea, UK | [4]Department of Industrial and Materials Science, Chalmers University of Technology, Gothenburg, Sweden | [5]School of Integrated Circuits, Peking University, Beijing, China | [6]Department of Chemical Engineering, University of Manchester, Manchester, UK | [7]Energy Innovation Centre, Warwick Manufacturing Group, University of Warwick, Coventry, UK | [8]School of Transportation Science and Engineering, Beihang University, Beijing, China

Correspondence: Hua Fan (h36fan@pku.edu.cn) | Xinhua Liu (liuxinhua19@buaa.edu.cn) | Rui Tan (rui.tan@swansea.ac.uk) | Jinhua Sun (jinhua@chalmers.se)

ABSTRACT

Sodium-ion batteries (SIBs) are emerging as a viable and cost-effective alternative to lithium-ion batteries, benefiting from sodium's high terrestrial abundance. However, their practical application is limited by rapid capacity fading stemming from structural instability during cycling and intrinsically sluggish Na$^+$ diffusion kinetics. High-entropy materials (HEMs), through configurational entropy maximization and multi-cation synergy, provide a promising strategy to stabilize structures and enhance the energy of SIB cathodes. This review focuses on the structural and chemical principles of key SIB cathodes—layered oxides and Prussian blue analogs—and critically evaluates high-entropy engineering strategies to performance enhancement. Mechanistic insights into entropy-driven performance enhancement are analyzed alongside current challenges and future research directions. The high-entropy strategy offers significant flexibility in cathode design, potentially overcoming conventional material limitations and accelerating commercialization. Although in its nascent stages, requiring extensive fundamental investigation, this analysis aims to guide the development of next-generation entropy-stabilized cathodes and advance SIB technologies.

1 | Introduction

Amid global efforts to achieve carbon neutrality, restructuring energy systems is crucial for mitigating the climate crisis. The International Energy Agency projects renewable source must supply over 85% of global electricity by 2025 [1–7]. As a major source of carbon emissions, transportation is undergoing rapid innovation, and the utilization rate of new energy is gradually increasing. Among them, power batteries are the core of electric vehicles and clean energy infrastructure [8–13], but they face performance, cost, safety, and sustainability constraints that hinder development [14–17]. Although lithium-ion batteries

(LIBs) dominate the market with featured high technical readiness levels (TRL, as shown in Figure 1 and Table 1), their scalability is limited by lithium's low crustal abundance (0.006 wt.%), geopolitical risks in cobalt and nickel supply chains, rising extraction costs, and inherent thermal runaway risks [32–38]. Surging demand (> 22% electric vehicle adoption) exacerbates market volatility, underscoring the need for resource-resilient alternatives [39–46].

SIBs offer a promising alternative because of sodium's high crustal abundance (2.74 wt.%, 420 times that of lithium), low cost, reduced polarization, and wide-temperature operability
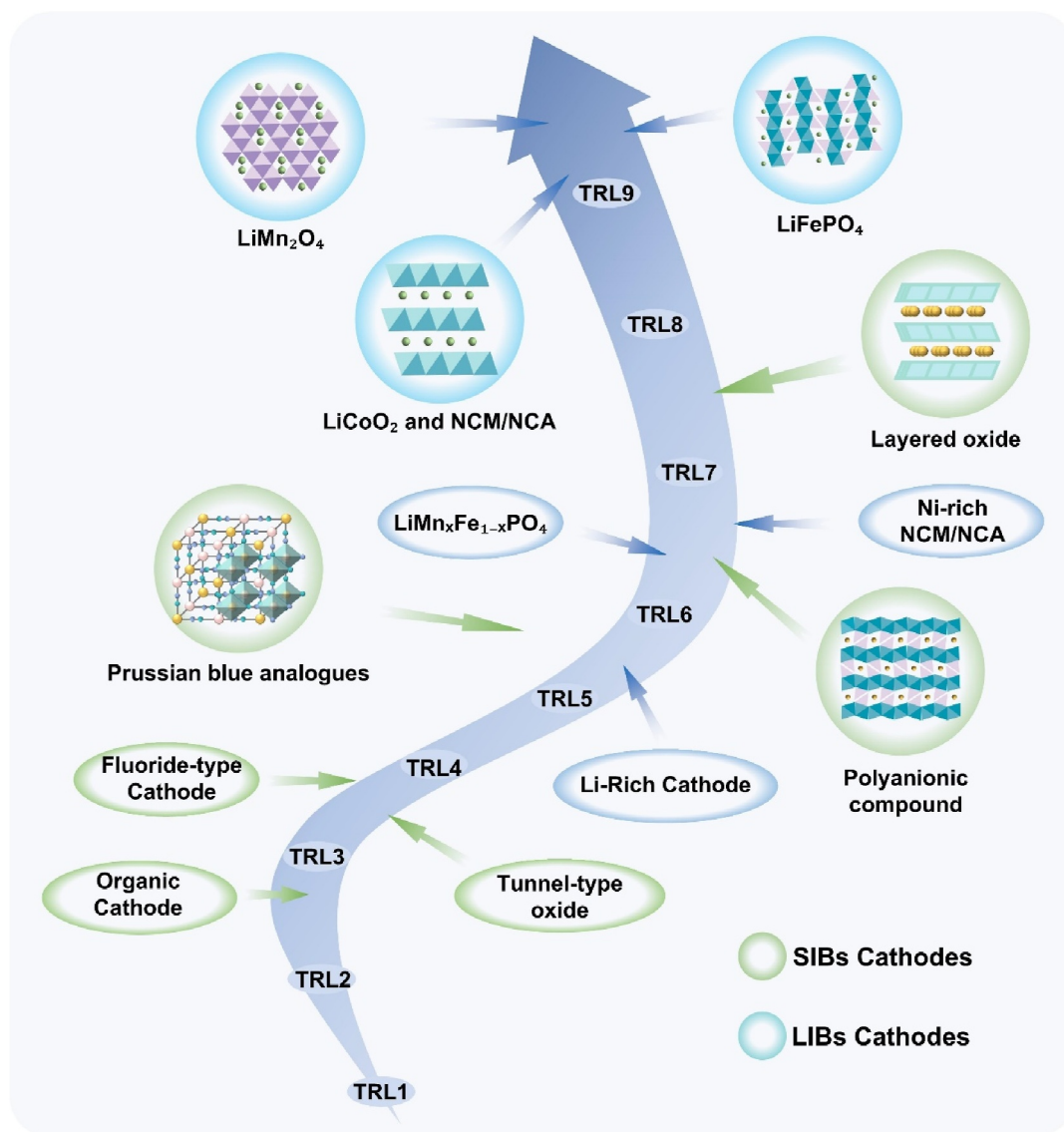
FIGURE 1 | TRL diagram of Li/Na ion battery cathodes. TRL definition [18]: TRL 1: Fundamental principles of a new electrochemical system/ material are discovered. TRL 2: A technological concept for a new electrochemical system/material is formulated. TRL 3: Laboratory proof-of-concept is completed, with key performance metrics preliminarily validated experimentally. TRL 4: A small-scale battery prototype is fabricated, and systematic evaluation of its physicochemical properties is completed in a laboratory environment. TRL 5: The battery prototype is tested under simulated real-world operating conditions; performance data can support preliminary feasibility analysis for specific application scenarios (e.g., consumer electronics and energy storage). TRL 6: Batch-stable production of kilogram-scale material is achieved and integrated into actual-size battery modules or packs; TRL 7: The battery system undergoes field demonstration and data collection in real end-use scenarios (e.g., pilot energy storage stations and test vehicles). TRL 8: Mass production processes are verified and finalized; the product obtains authoritative certifications for the target market and receives its first commercial orders. TRL 9: Stable high-volume production is achieved; the product is validated long-term in application, costs are competitive, and it holds a stable market share in the target market.

[40]. Paradoxically, conventional sodium-ion cathode materials, for example, layered transition metal oxides (LTMOs) and Prussian blue analogs (PBAs) (Figure 1 and Table 1), suffer from limited specific capacity, rapid capacity fading, and sluggish Na^+ diffusion kinetics. Transformative cathode design is thus essential for high-energy and long-cycle applications.

Although methods such as traditional doping have been used to modify SIBs cathodes simultaneously addressing phase transition and interfacial decay remains challenging. High-entropy doping overcomes the concentration limits and elemental exclusivity of traditional doping, achieving atomic-level synergy among multiple elements. This strategy not only generates unique properties beyond the sum of single elements but also imparts excellent thermal and structural stability, offering a new paradigm for bulk atomic control to achieve breakthrough performance improvements.

High-entropy materials (HEMs) typically refer to single-phase solid solutions formed by five or more principal elements (each with a molar fraction between 5% and 35%), whose high thermodynamic stability primarily stems from the mixing

TABLE 1 | Advantages and disadvantages of mainstream Li/Na-ion battery cathode materials and their TRL.

| Cathodes		Advantage	Disadvantage	TRL	Refs
LIBs	$LiCoO_2$	Discharge platform: 4.2–4.6 V (**3.7 V**)	Cycle life: > 500 cycles	9	[19]
		Energy density: 500 Wh kg^{-1} (**180–240 Wh kg^{-1}**)			
	NCM/NCA	Energy density: **180–300** Wh kg^{-1}	Thermal runaway: 220°C–250°C	9	[20]
		Low-temperature performance: > 70% capacity at −20°C			
	$LiMn_2O_4$	High safety performance	Energy density: **130–180 Wh kg−1**	9	[21]
			Cycle life: > 500 cycles		
	$LiFePO_4$	Cycle life: > 2000	Energy density: **130–160 Wh kg−1**	9	[22]
		High safety performance	Low-temperature performance: ~60% capacity at −20°C		
	$LiMn_xFe_{1-x}PO_4$	Energy density: 559 Wh kg^{-1} (**160–230 Wh kg^{-1}**)	Electrical conductivity:10^{-13} S cm^{-1}	6–7	[23]
		Low-temperature performance: > 75% capacity at −20°C			
	Ni-rich NCM/NCA	Energy density: 941.2 Wh kg^{-1}	Thermal runaway: 150°C–200°C	6–7	[24]
		High discharge plateau			
	Li-rich cathode	Energy density: 1100 Wh kg^{-1}	Voltage decay: 1–2 mV per cycle	5–6	[25]
		Cycle life: > 2000 cycles			
SIBs	Layered oxide	Energy density: 534 Wh kg^{-1} (**130–170 Wh kg^{-1}**)	Air sensitivity	7–8	[26]
		Mature preparation process	Poor structural stability		
	Prussian blue analogs	Theoretical specific capacity: 170 mAh g^{-1}	Energy density: 450 Wh kg^{-1} (**50–160 Wh kg^{-1}**)	5–6	[27]
			Cycle life: > 1000 cycles		
	Polyanionic compound	Cycle life: > 4000 cycles	Energy density: 405 Wh kg^{-1} (**90–130 Wh kg^{-1}**)	6–7	[28]
		High safety performance			
	Tunnel-type oxide	Stable structure	Energy density: ~90–130 Wh kg^{-1}	4–5	[29]
		Environmentally friendly	Specific capacity: 93mAh g^{-1} at 5C		
	Fluoride-type	Operating voltage: > 3.5 V	Complex preparation process	3–4	[30]
	Organic	Environmentally friendly	Electrical conductivity: 10^{-7} S cm^{-1}	2–3	[31]

Note: The bold values represent business data.

entropy-driven effect provided by the enormous configurational entropy (ΔS_{config}) [47]. The classical criterion originates from the field of high-entropy alloys, generally requiring $\Delta S_{config} \geq 1.5$ R (where $R = 8.314$ J·mol^{-1}·K^{-1}) [48]. It is worth noting that the high-entropy definition itself serves as a guideline for related research rather than a rigid "law." According to its foundational definition, strictly calculating configurational entropy should account for all elements (including minor elements or dopants with concentrations below 5%). However, in practice, due to the very low concentration of minor elements, their contribution to the total entropy value is negligible and does not affect the determination of the material's compliance with the essential nature of being high-entropy. Therefore, in most studies, including this work, to highlight the design focus and simplify analysis, the calculation of configurational entropy and the determination of the high-entropy threshold are typically based solely on the composition of the principal elements

($\geq 5\%$). Introducing small amounts of dopants ($< 5\%$) to optimize specific properties has become a common and effective strategy in high-entropy material design and does not contradict their core attributes as high-entropy materials. Leveraging the unique structural and thermodynamic features, HEMs enhance electrochemical performance and accelerate SIBs industrialization, driving significant academic and commercial interest within a wide range of fields [21, 49].

In the context of battery materials, four effects govern HEMs performance (Figure 2):

i. High-entropy effect: The core of this effect lies in the elevated configurational entropy (ΔS_{config}) introduced by the mixture of multiple principal elements. By contributing to the Gibbs free energy ($\Delta G = \Delta H - T\Delta S$), it significantly reduces the system's free energy at high
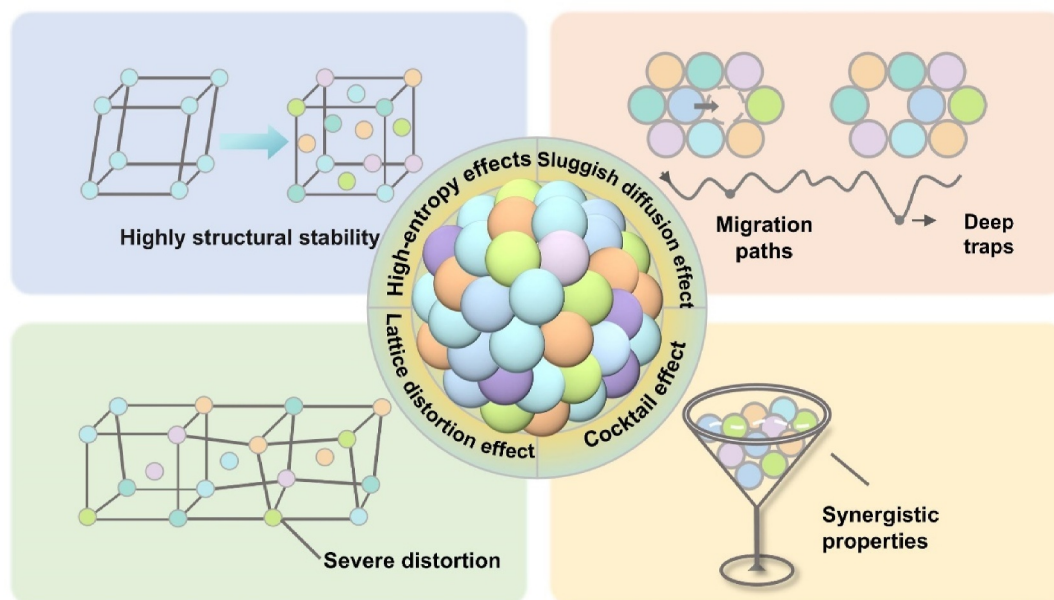
FIGURE 2 | Schematics illustrating four core mechanisms of HEAs including high-entropy effect, sluggish diffusion effect, lattice distortion effect, cocktail effect.

temperatures. From a macroscopic and statistical thermodynamic perspective, the high-entropy effect stabilizes single-phase multi-component solid solutions, effectively suppressing compositional segregation, metastable phase transitions, and the precipitation of ordered phases or simple compounds [50]. Consequently, the high-entropy effect provides the material with excellent intrinsic thermal and phase stability, forming the foundation for constructing homogeneous solid solutions and mitigating performance degradation often associated with multi-phase coexistence in conventional materials [51].

ii. Diffusion delay effect: From a dynamic perspective, the diffusion delay effect in HEMs originates from the sluggish diffusion of multiple ions and the interfacial atomic disparities [52]. This inhibits disordered metal migration and undesirable phase transitions. As a result, it mitigates battery volume expansion and capacity degradation, extending cycle life.

iii. Lattice distortion effect: It stems from cooperative mismatch in ionic radii, which induce localized distortions across the crystal lattice. These create ion transport barriers that facilitate efficient alkali-ion percolation. Simultaneously, the generation of surface defects and unsaturated coordination sites enhance Li^+/Na^+ adsorption and provide additional active sites for electrochemical reaction intermediates, thus improving overall reaction kinetics [53];

iv. Cocktail effect: When multiple elements coexist at the atomic scale, the complex interactions among their electrons—such as charge transfer, orbital hybridization, and coupling with lattice distortions—can induce unique and unpredictable properties that surpass a simple linear combination of the individual components' characteristics [54]. This effect adopts a microscopic and performance-

oriented viewpoint, focusing on the synergistic enhancement phenomenon of "the whole being greater than the sum of its parts" arising from the chemical interactions between elements. For example, specific multi-element combinations may confer upon the material high intrinsic electrical conductivity, exceptional catalytic activity, or unusual mechanical strength [55].

Collectively, the four effects form a comprehensive theoretical framework that underpins the unique advantage of HEMs in addressing the intrinsic limitations of conventional battery materials [56].

In SIBs high-entropy cathode materials, although research on high-entropy polyanionic compounds has recently emerged, LTMOs and PBAs exhibit more promising overall performance advantages over polyanionic compounds in the context of power battery applications [57–59]. High-entropy engineering enhances their structural stability and capacity through component modulation. LTMOs are susceptible to interlayer sliding and phase transitions during deep sodium insertion and extraction, whereas PBAs often suffer from structural defects and poor cycling performance [60]. The high-entropy approach has been shown to effectively suppress the inherent structural degradation mechanisms in these two material systems. In contrast, polyanion compounds typically possess open and stable three-dimensional frameworks, along with high thermal and electrochemical stability due to strong covalent bonding [61]. Consequently, the enhancement in structural stability achieved through multi-element doping is relatively limited. Their primary performance limitations are generally associated with low electronic conductivity and voltage or capacity constraints in certain systems. Although the high-entropy strategy may theoretically influence the electronic structure by modulating transition metal sites, its effectiveness in addressing key bottlenecks—such as intrinsic low

conductivity—has not been conclusively demonstrated. Moreover, the inherently robust framework of polyanion compounds may exhibit limited reliance on the lattice distortion and slow diffusion effects induced by high entropy [62]. Therefore, high-entropy LTMOs and high-entropy PBAs, due to their superior compositional tunability and lower industrialization costs, are more likely to facilitate the large-scale application of sodium-ion batteries in the field of power batteries.

Most existing reviews fail to systematically elaborate on how high-entropy strategies specifically tackle the application challenges encountered by cathode materials, which hinders the accelerated innovative application of such materials. Consequently, this review provides a forward-looking analysis of the structural basis and inherent limitations of LTMOs and PBAs. It systematically elucidates recent research progress in employing the high-entropy strategy to transcend these constraints, offering an in-depth analysis of the underlying performance enhancement mechanisms. Furthermore, the study summarizes the existing challenges and optimization pathways for HE-LTMOs and HE-PBAs, aiming to provide valuable insights for future research and accelerate the applications of high-entropy approaches in the design of SIB cathodes.

2 | High Entropy Layered Oxide Cathode Material

Among the numerous cathode materials for sodium-ion batteries, layered transition metal oxides (LTMOs) have garnered significant attention due to their high theoretical capacity and mature preparation processes. However, their structural instability limits further application. The introduction of the high-entropy strategy offers a new avenue for enhancing their overall performance. Next, this article will systematically elaborate on the structural characteristics, modification strategies, and performance enhancement mechanisms of high-entropy layered oxides.

2.1 | Infrastructure and Characteristics

Their 2D layered structure comprises transition metal–oxygen (TMO_2) slabs stacked by van der Waals/electrostatic forces, providing interlayer diffusion channels for reversible Na^+ deintercalation. LTMOs are typically formulated as Na_xTMO_2, and are structurally classified into P-type and O-type structures (Figure 3a). In P-type structures, Na^+ occupies trigonal prismatic sites, common in P2 (ABBA stacking) and P3 variants, whereas in O-type structures, Na^+ resides in the octahedral sites, as seen in O3 (ABCABC stacking) and O2 form [63]. "P" and "O" denote trigonal prismatic and octahedral Na^+ coordination, respectively, with numerals indicating oxygen-layers per unit cell. Na^+ content strongly influences the coordination environment, with high Na^+ favoring octahedral and low Na^+ favoring trigonal prismatic coordination [64].

Among these, O3- and P2-type LTMOs show particular prominence. O3-type LTMOs deliver high initial capacity and broad voltage plateaus but suffer from limited rate capability and cycle
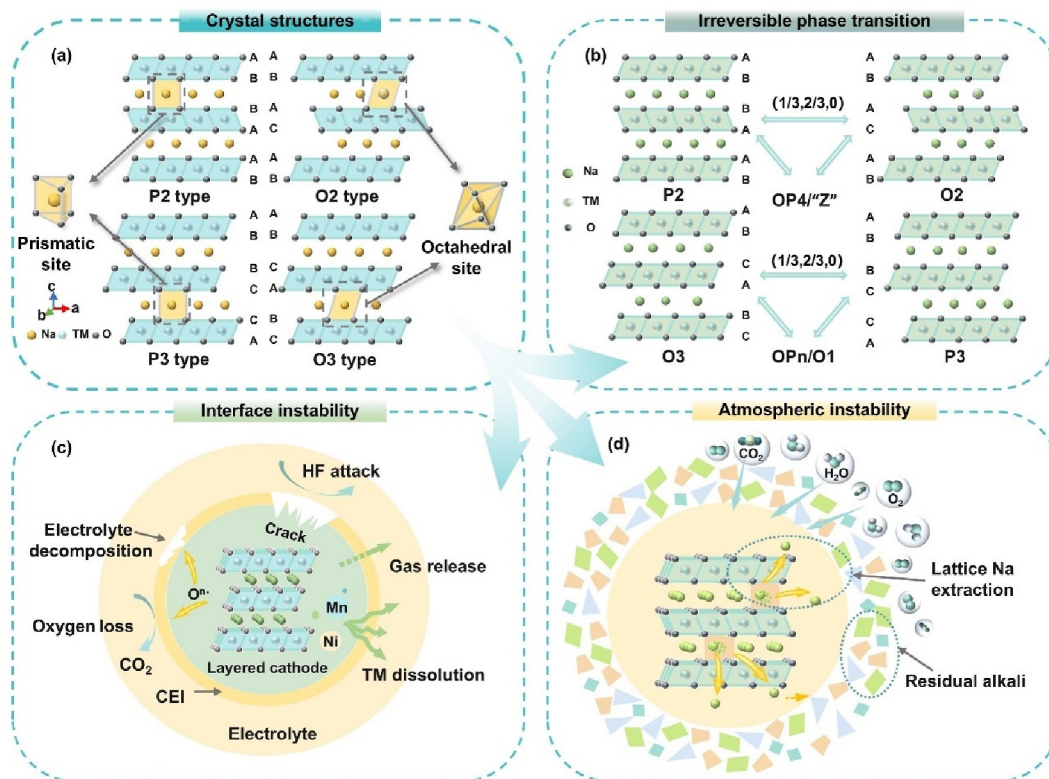
FIGURE 3 | Basic structure and main characteristics of LTMOs. (a) Crystal structure of different types of LTMOs. (b) Schematic diagram of phase transition instability in LTMOs. (c) Schematic diagram of poor interfacial stability between LTMOs electrode and electrolyte. (d) Schematic diagram of atmospheric instability in LTMOs.

stability. Conversely, P2-types provide superior rate performance and cyclability through open frameworks, yet their low Na^+ content reduces capacity and induces irreversible phase transitions with lattice distortion [65]. Conventional strategies including cation doping, structural tuning, and biphasic engineering partially mitigate these issues. Nonetheless, persistent issues, for example, irreversible phase transformations, interfacial degradation, and poor air stability performance, continue to hinder the practical deployment of LTMOs in SIBs.

During the electrochemical cycling, repeated Na^+ deintercalation induces lattice stress accumulation in LTMOs, leading to irreversible phase transitions and structural degradation. As illustrated in Figure 3b, P2-type materials undergo interlayer sliding at high potentials, with the oxygen stacking sequence shifting from ABBA to ABACAB. This transition is accompanied by the Na^+ migration from trigonal prismatic positions to octahedral positions, ultimately forming a thermodynamically stable O2 phase or transforming into OP4/"Z" phase [66]. In contrast, O3-type materials follow more complex multi-step phase transition pathways, such as O3–P3–O′3 or O3–P3–OPn/O1, causing gradual distortion and eventually structural collapse. These phase transitions not only compromise structural integrity but also induce microcracking within the electrode, severely impairing cycling stability [60, 67].

Simultaneously, high-voltage cycling exacerbates side reactions at the electrode–electrolyte interface. Oxidative decomposition of the electrolyte generates acidic species that corrode the TM-O layers, resulting in metal ion dissolution, lattice oxygen loss, and the formation of a non-uniform cathode electrolyte interphase (CEI) film (Figure 3c). This non-uniform CEI introduces localized charge imbalance, evaluating Na^+ transport resistance and inducing safety hazards. Volume changes during cycling further amplify the surface stress, leading to nanoscale cracking that exposes fresh active sites, perpetuating a feedback cycle of interfacial degradation and parasitic reactions [68].

Additionally, the air sensitivity of LTMOs presents significant challenges for both material synthesis and storage. Their open layered structures and surface basicity promote reactions with atmospheric H_2O and CO_2, resulting in the formation of insulating compounds such as NaOH and Na_2CO_3 (Figure 3d). These surface deposits block Na^+ diffusion channels and degrade structural integrity. More critically, water-induced Na^+/H^+ exchange reactions irreversibly consume active sodium sites, lowering sodium content and causing permanent capacity decay [69–71].

2.2 | High Entropy Strategy and Application

To address the limitations of LTMOs, various modification strategies, including ion doping, structural design, surface coating and process optimization, have been explored with notable progress in performance enhancement [72–75]. However, the industrial implementation remains constrained by the synthesis complexity, low yield, and limited cost-effectiveness. With rational design, high-entropy cathode materials featuring equimolar multi-element compositions offer cost reduction and enhanced sustainability over traditional battery cathodes. The high-entropy strategy integrates entropy stabilization and multi-element doping effects, offering a robust approach to mitigating irreversible phase transitions, interfacial instability, and air sensitivity [58, 76–78].

2.2.1 | Phase Transformation Stabilization Strategies

Irreversible phase transitions remain a major obstacle to the large-scale commercialization of LTMOs in SIBs. For instance, a typical O3-type LTMO usually undergoes a complex and continuous O3–P3–O′3 phase transition with significant lattice distortion during the charging cycle, resulting in significant structural degradation and rapid capacity loss [79]. Stabilizing the phase evolution process is therefore essential for improving the electrochemical performance of layered oxide cathodes and enabling the practical deployment of SIB technology. Among various stabilization strategies, high-entropy doping strategy offers a robust pathway to enhancing the long-term structural and electrochemical stability of LTMO cathodes, with strong implications for advancing the industrial viability of SIBs [80].

Employing high-entropy configurations to modulate the local electronic environment within TM layers offers an effective strategy to promote reversible phase transitions in LTMOs. High-entropy doping enhances electron localization around oxygen atoms, thereby reducing the electron density in Na-O bonds and weakening the electrostatic interaction between electrons and interlayer Na^+. This modification stabilizes the TM-O framework and facilitates faster Na^+ diffusion. In the system of $NaNi_{0.2}Fe_{0.2}Mn_{0.35}Cu_{0.05}Zn_{0.1}Sn_{0.1}O_2$(NFMCZS), the strong charge localization effect (Figure 4c) induced by inactive elements such as Sn/Mn/Zn firmly anchors the coordinated oxygen atoms in the TM layer, effectively suppressing the slippage of the TMO_2 layer during Na^+ deintercalation, and avoiding irreversible phase transitions and structural collapse (Figure 4b). In addition to enhancing the stability of the transition metal framework, Mn/Zn/Sn can also stabilize the valence state, while Ni/Fe/Cu plays a role of charge compensation, which is confirmed in the calculation of synchrotron radiation hard x-ray absorption spectrum (XAS) and charge localization function (Figure 4d). Rietveld refinement of XRD pattern of NFMCZS and NFM ($NaNi_{0.2}Fe_{0.2}Mn_{0.6}O_2$) cathode after 300 cycles at 1.0 C (Figure 4a) showed that the NFMCZS cathode achieved a reversible phase transition of O3–P3–O3 during the cycle (Figure 4e), whereas the NFM cathode experienced a complex phase transition of O3–P3–P′3–O3+P3. Compared with NFM material, the volume strain is 0.11% after 300 cycles, and the capacity retention rate increases from 24% to 87% after 500 cycles at 3.0 C [81]. Similarly, the study of the O3–$Na_{0.9}Ni_{0.2}Fe_{0.2}Co_{0.2}Mn_{0.2}Ti_{0.15}Cu_{0.05}O_2$(NaNFCMTC) supports the above view again. The improvement of electron localization around oxygen leads to the significant enhancement of Ti-O bond, which enhances the stability of transition metal framework in high entropy system (Figure 4f). In addition, the increase of electron localization also reduces the electron density between Na–O bonds, which significantly reduces the electrostatic interaction between electrons and interlayer Na^+,
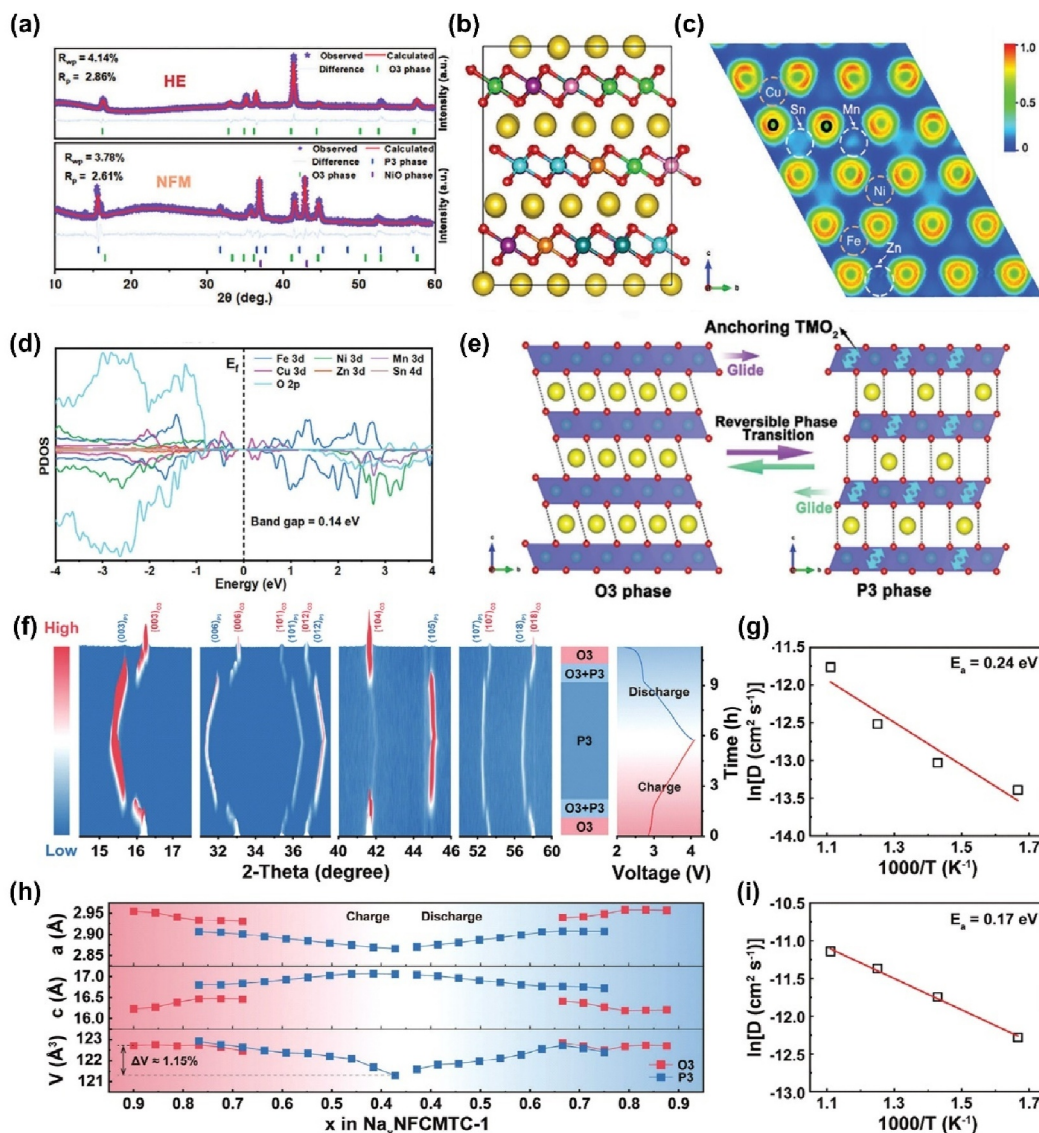
FIGURE 4 | (a) Rietveld refinement of XRD pattern of NFMCZS and NFM cathode after 300 cycles at 1.0 C. Reproduced with permission [81]. Copyright 2024 Wiley. (b) The optimized crystal structure of NFMCZS. Reproduced with permission [81]. Copyright 2024 Wiley. (c) Electron localization function (ELF) of valence electrons viewed along (001) lattice planes of NFMCZS. Reproduced with permission [81]. Copyright 2024 Wiley. (d) Partial density of states (PDOS) of metal d and O2p orbitals of NFMCZS. Reproduced with permission [81]. Copyright 2024 Wiley. (e) Schematic diagram of the O3–P3–O3 reversible phase transition of NFMCZS. Reproduced with permission [81]. Copyright 2024 Wiley. (f) In situ XRD patterns of NaNFCMTC corresponding voltage profile during the first charge–discharge at 0.1 C in the voltage range of 2.2–4.1 V. Reproduced with permission. [82]. Copyright 2024 Wiley. (h) Evolution of lattice parameters (a-axis, c-axis, and volume) calculated from the in situ XRD data. Reproduced with permission [82]. Copyright 2024 Wiley. Corresponding Arrhenius plots of diffusion coefficients in NaNFCMTC −1 are presented in (g) O3 and (i) P3 phase, from which Na^+ migration energy barriers of 0.24 and 0.17 eV are obtained, respectively. Reproduced with permission [82]. Copyright 2024 Wiley.

promotes the rapid diffusion of Na^+ (Figure 4g,i), and delays the evolution from O3 phase to P3 phase. The NaNFCMTC−1 TMO_2 slab synthesized by the researchers shrank (Figure 4h), realized rapid Na^+ transmission through the expanded Na^+ transmission channel, and realized low Na^+ migration energy in the process of Na^+ (de) intercalation [82].

Complementary to integrity studies of multiple doped metals, targeted studies on the specific metals may offer a more

insightful approach to unraveling the mechanisms of material enhancement. In the study of Sn^{4+} gradient doping regulation, the $NaNi_{0.4}Mn_{0.3-x}Fe_{0.1}Ti_{0.1}Sn_xLi_{0.05}Sb_{0.05}O_2$ system exhibits a solid solution reaction characteristic dominated by the P3 phase. As the content of Sn^{4+} increases, the O3–P3 phase transition process becomes smoother (Figure 5a), the two-phase region of O3/P3 narrows, and the ionicity of the transition metal–oxygen bond increases simultaneously. The dominant P3 phase has an enlarged layer spacing and an open ion diffusion channel, which
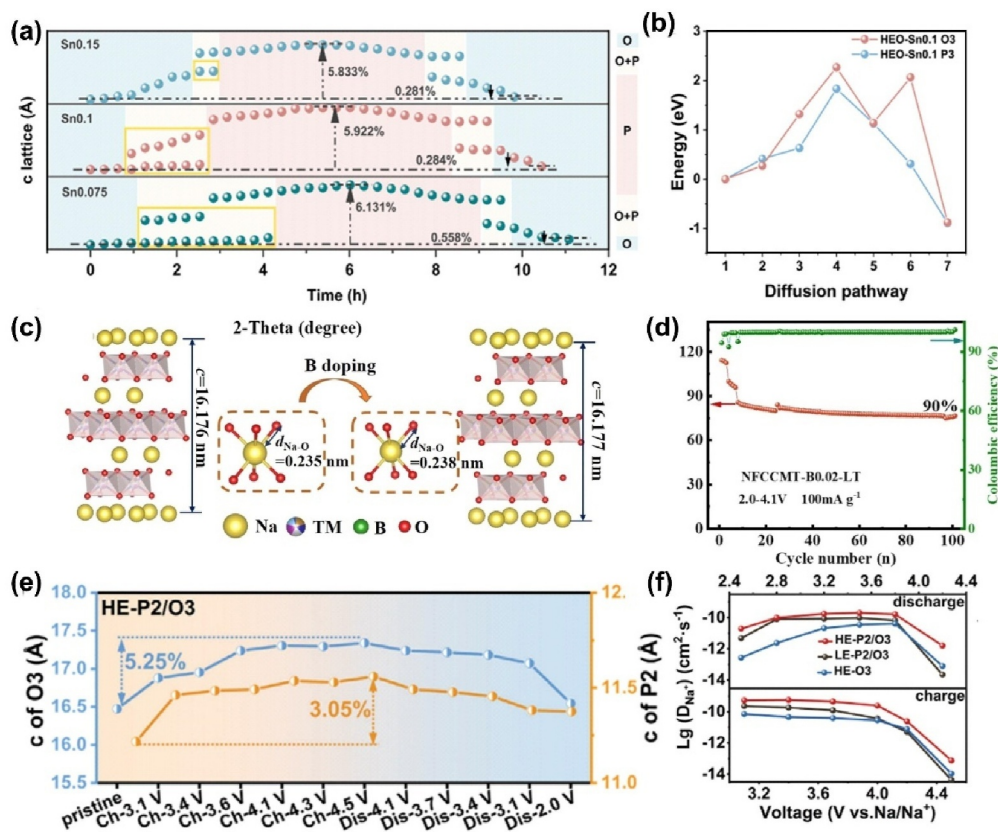
FIGURE 5 | (a) The comparison of c-lattice parameters changes of HEO-Sn$_{0.15}$, HEO-Sn$_{0.1}$, and HEO-Sn$_{0.075}$ electrode materials in the first cycle. Reproduced with permission [83]. Copyright 2025 Elsevier. (b) The illustration of the Na$^+$ ions migration energy barriers of O3-type and P3-type phases structure. Reproduced with permission [83]. Copyright 2025 Elsevier. (c) Structure diagram of NFNCCMT and NFNCCMT-B$_{0.02}$ models. Reproduced with permission [84]. Copyright 2024 Elsevier. (d) Low-temperature cycling performance of NFNCCMT-B$_{0.02}$ at 1 C. Reproduced with permission [84]. Copyright 2024 Elsevier. (e) The changes of lattice parameter c in HE-P2/O3. Reproduced with permission [85]. Copyright 2024 Wiley. (f) Comparison of D$_{Na+}$ among LE-P2/O3, HE-P2/O3, and HE-O3 in the first cycle based on Galvanostatic Intermittent Titration Technique tests. Reproduced with permission [85]. Copyright 2024 Wiley.

reduces the sodium ion migration barrier (Figure 5b) [83]. It is worth noting that the synergistic effect of B doping and high-entropy strategy has been verified in the NaFe$_{0.2}$Co$_{0.15}$Cu$_{0.05}$-Ni$_{0.2}$Mn$_{0.2}$Ti$_{0.2}$B$_{0.02}$O$_2$ (NFNCCMT-B$_{0.02}$) material. High-entropy doping effectively suppresses phase transitions and volume changes during the cycling process, enhancing the stability of the structure (Figure 5c). Meanwhile, strong covalent B–O bond formation causes the transition metal layer to contract, triggering outward expansion of the sodium–oxygen layer. This expansion increases the sodium interlayer spacing, thereby stabilizing the P3 phase region, which facilitates rapid sodium-ion diffusion and enhances structural rigidity. Thus, this synergistic doping exhibit excellent cycle performance (Figure 5d) and rate performance in a wide temperature range (−20°C–60°C) [84]. Breaking through the traditional single-phase research paradigm, multiphase high-entropy systems exhibit unique advantages. By regulating the weighted average ionic radius (WAIR = 0.583–0.637 Å) of transition metals, a precise P2/O3 dual-phase structure can be constructed. The disordered distribution of Mn/Cu/Ti/Sn effectively suppresses the irreversible O3−P3 and P2−O2 phase transitions and enhances the Na$^+$ migration rate (Figure 5f) while the lattice orientation difference between the two phases further hinders interlayer slip and lattice volume strain (Figure 5e) [85].

2.2.2 | Interface Stabilization Strategies

In addition to suppressing phase transitions, the high-entropy strategy also demonstrates significant advantages in enhancing the stability of the electrode-electrolyte interface. Under high-voltage conditions, interfacial side reactions and oxygen loss are major contributors to performance degradation. Under high-voltage conditions, the anionic redox reactions in LTMO materials exhibit significant irreversibility. Released oxygen forms reactive oxygen species (ROS) that react with the electrolyte, catalyzing electrolyte degradation and gas evolution. These processes severely compromise interfacial stability and cycling performance, leading to battery swelling or even thermal runaway [86]. Therefore, regulating the redox stability of oxygen in the layered oxide lattice, suppressing oxygen migration, and reducing persistent oxygen loss and irreversible structural degradation are critical for enhancing interfacial and cycling stability. Additionally, volumetric fluctuations during cycling induce nanoscale cracks on the electrode surface, allowing electrolyte infiltration into these cracks and triggering cascading detrimental side reactions that exacerbate interfacial instability [87].

High-entropy doping can modulate the electronic structure and strengthen the lattice framework of LTMOs, inhibiting TM

dissolution, lattice oxygen release, and crack formation in high-voltage regimes, thereby improving cycling stability and battery safety [88, 89]. Inducing high desodation state electronic structure disorder (ESD) through entropy enhancement strategies can effectively address the oxygen stability issue of high-voltage cathode materials. $NaCu_{0.1}Ni_{0.25}Co_{0.15}Mn_{0.35}Li_{0.05}Ti_{0.05}Sn_{0.05}O_2$ system (CNCMLTS) have shown that the ESD mechanism (Figure 6c,d) effectively inhibits the mobility of oxygen at the lattice interface and controls the oxygen activity (Figure 6b), stabilizes the redox behavior of lattice oxygen, raising the oxygen migration energy barrier to 1.85 eV. Compared with other configuration entropy, the cation disorder caused by high-entropy components perturb the redox boundaries and inhibit the formation of the harmful O′3 phase. This material exhibits excellent cycling stability (Figure 6a) and rate performance [90].

In the P2-type manganese-based cathode (HE-NMCO) system, high-entropy effect has been confirmed to optimize the reversibility of oxygen anion redox. High-entropy configuration enhances the stability of lattice framework, inhibits the movement of lattice oxygen, and achieves sustainable reversible oxygen activity by regulating the chemical properties of the local environment, reduces the stress concentration at the grain boundaries, reduces the lattice distortion and simultaneously promotes the Na^+ migration. Furthermore, various transition metal elements in HE-NMCO act synergically, promoting reversible oxygen anion redox reactions, reducing the formation of intramolecular cracks [92]. Similarly, the $Na_{2/3}Li_{1/6}Fe_{1/6}Co_{1/6}Ni_{1/6}Mn_{1/3}O_2$ system enhances the structural stability of the host lattice by inducing the superlattice structure through Li doping. The superlattice structure formed by doping lithium ions in the transition metal layer helps stabilize the host structure and promotes the rapid diffusion of sodium ions during the charging and discharging process. The stabilizing effect of high entropy and superlattice effectively inhibits the phase transition (Figure 6e–g) and irreversible oxygen-redox reactions of the material at high voltage, thereby significantly improving the cycle stability and fast charging of sodium-ion batteries [91].

Based on high-entropy doping mainly with transition metals, introducing other metals with synergistic effects (such as Li/Mg/Sb/Sn/F, etc.) for doping is also an innovative strategy to improve the interface stability. Ti/Sb to replace strategy in $NaNi_{0.35}Fe_{0.2}Mn_{0.3}Ti_{0.1}Sb_{0.05}O_2$ (NFMTS) system brought the double effect, The introduction of Ti^{4+} expands the interlayer spacing of the (101) crystal plane and promotes the insertion/deinsertion of sodium ions. Meanwhile, Sb^{5+} exerts a significant constraining effect on the surrounding oxygen ions through its
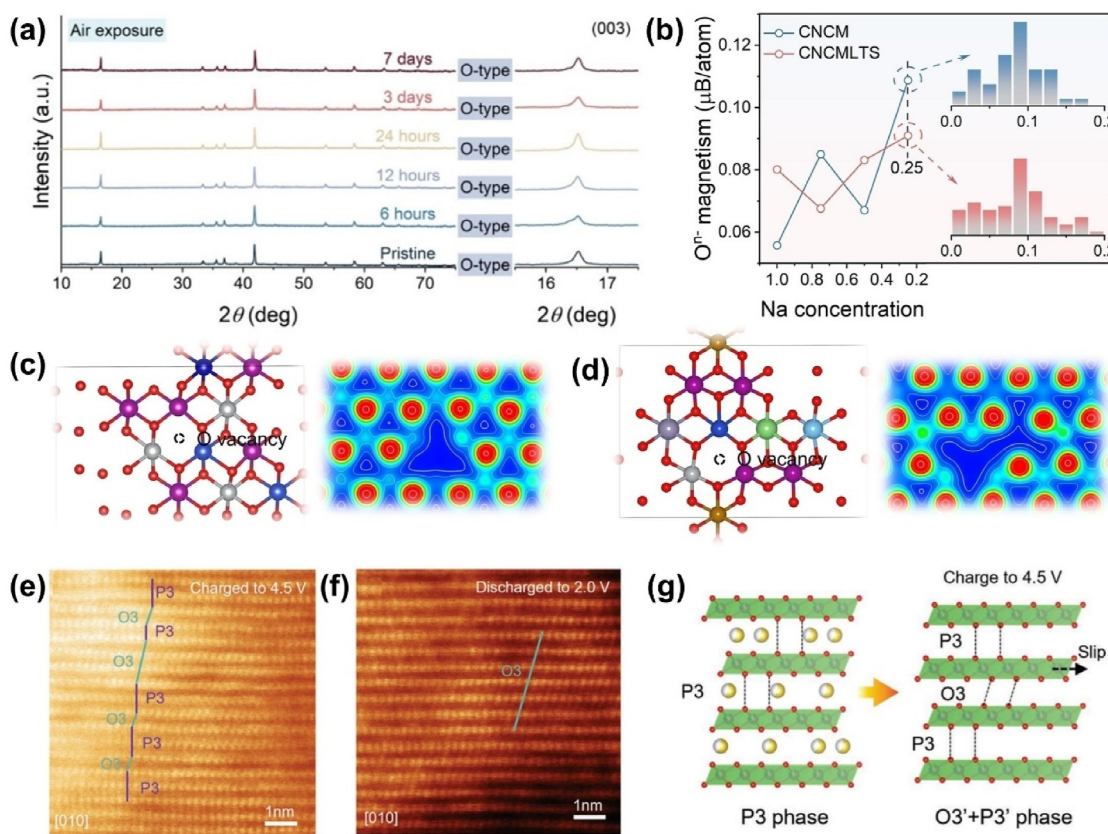
FIGURE 6 | (a) XRD patterns of CNCMLTS powders aging for different times upon exposure to an ambient air environment. Reproduced with permission [90]. Copyright 2025 Wiley. (b) Oxygen magnetism of CNCM and CNCMLTS at different concentration. Reproduced with permission [90]. Copyright 2025 Wiley. Crystal structures and the corresponding charge density contours of (c) CNCM and (d) CNCMLTS. Reproduced with permission [90]. Copyright 2025 Wiley. Ex situ HR-TEM image of NaLFCNM at (e) 4.5 V state and (f) 2.0 V state. Reproduced with permission [91]. Copyright 2022 Wiley. (g) Schematic illustrations of the whole phase evolution of NaLFCNM upon charge and discharge. Reproduced with permission [91]. Copyright 2022 Wiley.

strong electron delocalization field (Figure 7b), enhances the covalent property of the TM–O bond, inhibits the redox activity of oxygen, and alleviates the irreversible structural degradation and phase transition (Figure 7a) caused by the continuous loss of oxygen ions, Thereby enhancing the cycling stability of the material [93]. In the HE-CFMO system, Li/Mg/Ti co-doping demonstrates structural optimization effects on LTMOs. The partial substitution of Na by Li (Na: Li = 4:1) in the sodium layer not only reinforces interlayer connectivity between adjacent TM layers and stabilizes Na^+ diffusion pathways but suppresses the Jahn–Teller effect through valence elevation of Mn, synergistically enhancing the structural stability of the layered framework. Mg/Ti act as structural anchors, reducing the lattice distortion rate to 0.32% while effectively stabilizing the layered architecture and suppressing ion migration coupled with

structural deformation. The synergistic effects of high-entropy doping endow the TM layers with homogeneous elemental and stress distribution (Figure 7c), establishing a compact structural framework that effectively suppresses the formation of intragranular cracks and structural degradation. In stark contrast, the non-uniform atomic strain distribution in CFMO (Figure 7d) suggests an inherently unstable lattice structure, which is susceptible to phase transitions and lattice distortions. The valence state variation of Mn leads to significant structural deformation and crack propagation in the CFMO cathode during discharge, thereby severely impeding the diffusion and storage capability of Na^+ ions [94].

In addition to emphasizing the structural stability of the lattice, the compatibility between the electrode and the electrolyte must
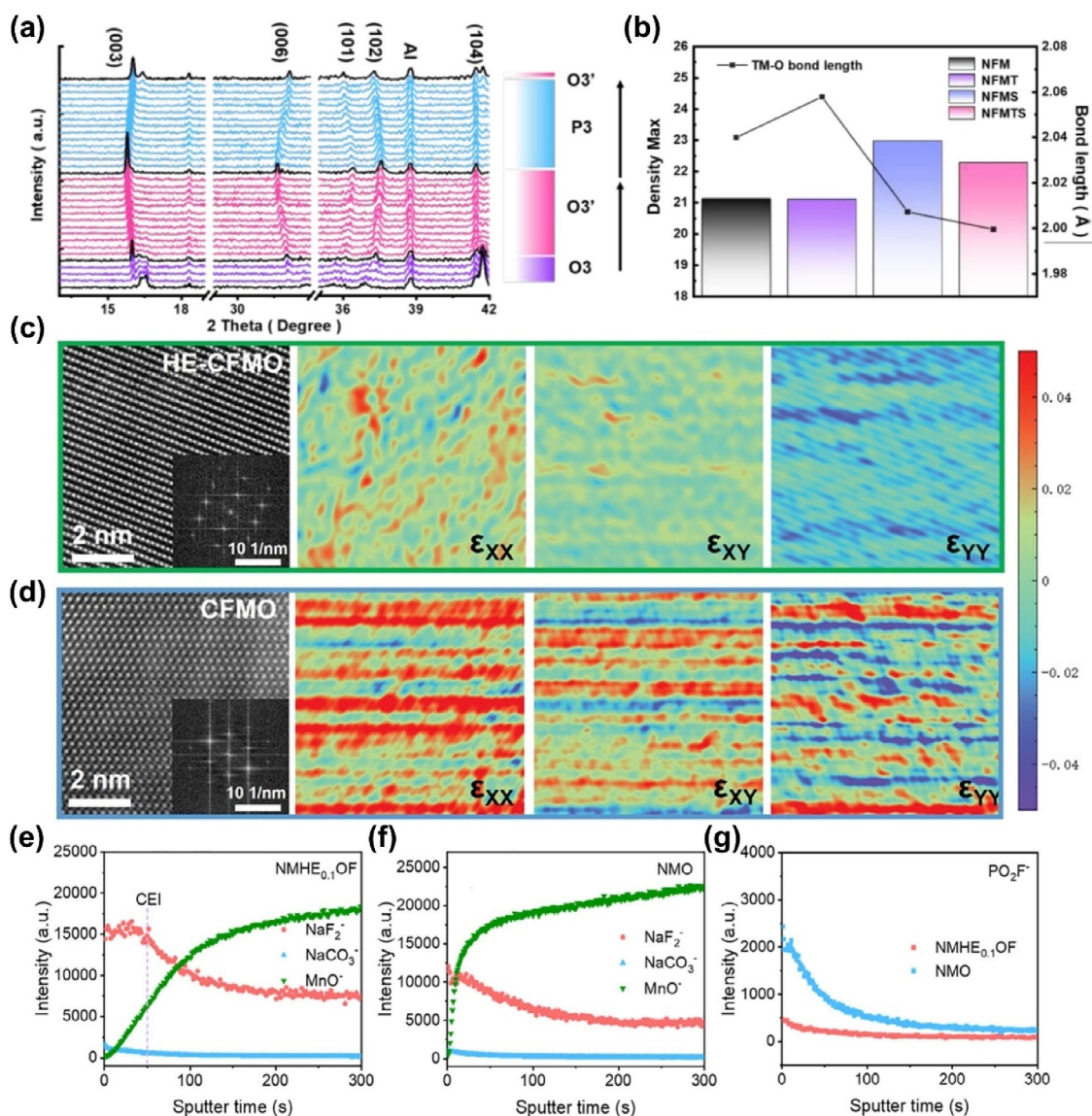
FIGURE 7 | (a) In situ XRD patterns collected during the galvanostatic charge/discharge process of NFMTS at 0.3 C, 1.9–4.1 V. Reproduced with permission [93]. Copyright 2024 Royal Society of Chemistry. (b) Combined bar and line graph of the maximum average electron density and TM-O bond lengths. Reproduced with permission [93]. Copyright 2024 Royal Society of Chemistry. HAADF images and the corresponding atomic strain distribution mapping of (c) HE-CFMO and (d) CFMO, where the red color in the analysis represents tensile strain, and the blue represents compression strain. ε_{XX}, ε_{XY}, and ε_{YY} represent horizontal normal strain, shear normal strain, and vertical normal strain, respectively. Reproduced with permission [94]. Copyright 2024 Wiley.

also be given critical attention. In the fluorine-containing high-entropy layered oxide $NMHE_{0.1}OF$ (P′2: $Na_{0.59}Mn_{0.90}Ti_{0.02}$-$Cu_{0.02}Ni_{0.02}Co_{0.02}Fe_{0.02}O_{1.95}F_{0.05}$) system, undoped NMO experiences severe and irreversible structural degradation and capacity attenuation during charge-discharge cycles due to the incompatibility between the electrode and the electrolyte. However, the strategies of high-entropy doping and fluorine doping effectively mitigate the contraction/expansion of the transition metal layer during these cycles. ToF-SIMS analysis (Figure 5e,f) indicates that, compared with NMO, NMHE0.1OF exhibits a higher content of inorganic components, which contribute to the formation of a dense and stable CEI layer on the electrode surface. This layer effectively passivates the electrode surface, thereby suppressing the decomposition of ether-based electrolytes under high-voltage conditions. Meanwhile, the PO_2F^- signal intensity in NMHE0.1OF is significantly lower than that in NMO (Figure 5g), indicating reduced HF generation. This leads to the formation of a more stable and denser CEI layer, enhancing the compatibility between the electrode and the electrolyte and minimizing side reactions such as electrolyte decomposition and gas evolution [95].

2.2.3 | Air Stabilization Strategies

Beyond stability during electrochemical cycling, the material's tolerance to atmospheric conditions during storage and electrode preparation is another critical factor limiting the practical application of LTMOs. Enhancing the material's intrinsic inertness to air is a necessary step for achieving its scaled-up production and application. When exposed to the atmosphere for extended periods, LTMOs cathode materials tend to react with moisture, carbon dioxide, and oxygen present in the air. These reactions can lead to the dissolution of sodium ions from the crystal lattice, resulting in irreversible capacity loss [96, 97]. Concurrently, water molecules facilitate Na^+ dissolution through Na^+/H^+ ion exchange, promoting the formation or structural transformation of hydrated phases. Furthermore, alkaline compounds generated on the material surface may induce gelation during electrode slurry preparation, complicating the coating process. These phenomena can potentially increase battery internal resistance and gas evolution, hinder Na+ and electron transport, and ultimately degrade overall battery performance [98]. Therefore, maintaining and enhancing structural stability as well as promoting the rapid diffusion of sodium ions are important directions for improving the air stability of LTMOs. In traditional strategies, the main means to enhance air stability are elemental doping and surface coating. However, the application of surface coating is constrained by factors such as complex procedures, uneven coating distribution, and high costs, which hinder its practical implementation [99].

In the context of doping strategies, doping elements can be categorized into active and inactive elements based on their redox activity. Active elements, including Ni, Fe, Mn, and Cu, serve a functional regulatory role by providing charge compensation during sodium ion intercalation and deintercalation, thereby significantly improving the material's specific capacity. This has been validated in both the NFMTS

($NaNi_{0.3}Fe_{0.2}Mn_{0.2}Ti_{0.15}Sn_{0.15}O_2$) [100] and Na_xLi_y ($Na_{0.9}Li_{0.1}$-$Ni_{0.4}Fe_{0.2}Mn^{2+}_{0.4}Ti_{0.04}Mn^{4+}_{0.04}Mg_{0.02}O_{1.9}F_{0.1}$) [101] systems. Conversely, inactive elements such as Ti and Sn contribute to structural stabilization by inhibiting structural evolution during charge–discharge cycles, optimizing electron conduction pathways, and thus markedly enhancing electron transport efficiency and structural stability. Notably, Sn^{4+}, because of its unique electronic configuration, avoids hybridization with the O 2p orbital, further strengthening the ionic character of the Ni–O bond and elevating the redox potential of Ni. These mechanisms collectively enable the NFMTS material to exhibit superior air stability (Figure 8a). Even after 80 days of air exposure (Figure 8b), although the specific capacity decreases by approximately 30%, it can be restored to 81.9% of its initial value through simple secondary annealing, accompanied by a significant increase in initial Coulombic efficiency to 95.9% [100]. Inactive elements such as Mn^{4+} and Mg enhance charge localization, effectively suppressing interlayer slippage and irreversible phase transitions, thereby improving both structural and air stability. Furthermore, the incorporation of Li in the Na_xLi_y system not only expands interlayer spacing to facilitate rapid sodium ion diffusion but also creates Na vacancies, which further enhance structural stability and oxidation resistance while inhibiting unnecessary reactions in air, demonstrating excellent air stability and capacity retention rate (Figure 8e). After 30 days of air exposure (Figure 8c,d), the XRD pattern of the $Na_{0.9}Li_{0.1}$ cathode reveals negligible impurities [101].

Al exhibits effects similar to those of Li, which reinforcing the TM–O bond, inhibiting TM layer slippage, and enhancing air stability. In the $O3-Na_{0.85}Li_{0.1}Al_{0.02}Sn_{0.08}Cu_{0.1}Ti_{0.1}Ni_{0.3}Mn_{0.3}O_2$ (HEO) system, high-entropy doping effectively preserves the covalency of the TM–O bond, maintains electron localization, and stabilizes interlayer oxygen charge, thereby preventing structural collapse caused by uneven O–O repulsion. Additionally, doping with inactive ions mitigates Jahn–Teller distortion induced by Ni^{3+} and suppresses the formation of the P′3 phase. Low oxidation state ion doping reduces interlayer oxygen charge, leading to sodium layer contraction and enhanced Na-O bond strength (Figure 8g), which suppresses sodium loss and water erosion while improving air stability. After 15 days of air exposure, HEO demonstrates minimal active sodium ion loss and alkaline compound formation (Figure 8f). By contrast, the control sample NFM ($O3–Na_{0.85}Ni_{0.3}Fe_{0.2}Mn_{0.5}O_2$) generates substantial alkaline compounds within 5 days, resulting in a capacity retention rate of only 66.03%, significantly lower than the 96.12% retention rate observed in the HEO system [102].

Based on element doping, combining high-entropy doping with other strategies may achieve collaborative optimization. For example, the combination of the high-entropy, single-crystal, and bipolar-triad strategies applied to the $O3-Na$ ($Fe_{1/6}Co_{1/6}Ni_{1/6}Mn_{1/6}Ti_{1/6}$) Li_xO_2 high-entropy system effectively mitigated the local structural changes during sodium-ion (de)intercalation. Combined with the single crystal structure, it further promotes the rapid transport of sodium ions in the system, reduces the diffusion distance, and thereby enhances the electrochemical performance (Figure 8g,h). Notably, the biphasic strategy ensures
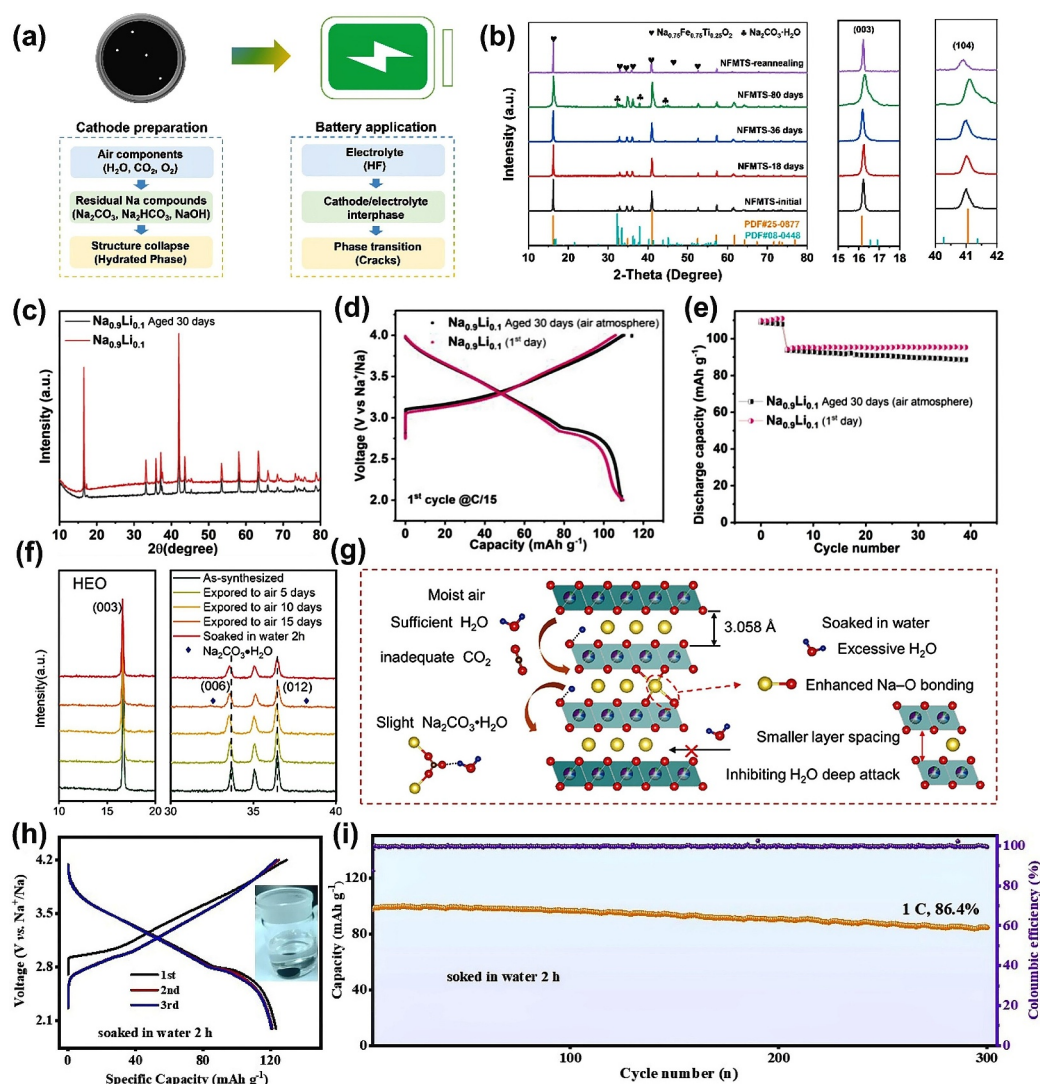
FIGURE 8 | (a) Schematic diagram of the challenges faced by layered oxides exposed to humid air from the outside to the inside. Reproduced with permission [100]. Copyright 2025 Elsevier. (b) XRD patterns of the TS, TS-Air and TS-Re. Reproduced with permission [100]. Copyright 2025 Elsevier. (c) XRD pattern of initial and aged $Na_{0.9}Li_{0.1}$. Reproduced with permission [101]. Copyright 2023 Wiley. (d) Comparison between the first cycle of aged $Na_{0.9}Li_{0.1}$ and that of the initial $Na_{0.9}Li_{0.1}$ (2–4 V). Reproduced with permission [101]. Copyright 2023 Wiley. (e) Comparison of capacity retention of $Na_{0.9}Li_{0.1}$ during cycling at 0.5 C discharge rate (initial at 0.06 C). Reproduced with permission. [101] Copyright 2025 Wiley. The XRD patterns for different exposure times to air and soaked in water of (f) HEO. Reproduced with permission. [102] Copyright 2025 Wiley. The mechanism demonstrations of (g) HEO exposed to air and soaked in water. Reproduced with permission. [103] Copyright 2024 Elsevier. (h) The charge and discharge curves of the water-soaked $NFCNMTL_{1/6}$ for the first three cycles at 0.1 C. Reproduced with permission. [103] Copyright 2024 Elsevier. (i) The cycling performance of water-soaked $NFCNMTL_{1/6}$ electrode at 1C. Reproduced with permission [103]. Copyright 2024 Elsevier.

strong cyclic stability and excellent durability (Figure 8i) against air exposure and water immersion by introducing $LiCoO_2$ (similar to $LiTMO_2$), which enhances the stability of the host framework, reduces water sensitivity, and prevents electrolyte erosion [103].

2.3 | Performance Improvement Mechanism

High-entropy doping strategies significantly enhance the comprehensive performance of LTMOs through multidimensional synergistic mechanisms. To address irreversible phase transitions, structural modulation is achieved via high-entropy configurations and elemental synergy. Introducing transition metal elements with distinct functionalities forms a disordered high-entropy framework, leveraging thermodynamic advantages of high configurational entropy to reduce energy barriers for reversible phase transitions. Concurrently, the disordered lattice environment delays and suppresses irreversible phase transitions typical in conventional LTMOs [104, 105]. Doping element selection should extend beyond transition metals, prioritizing alkali and light metals. In addition, other specific metal elements may also offer distinct advantages. Redox-active Ni/Fe/Cu/Co/Mn^{2+} ions act as charge-compensation elements to boost capacity; Non-redox-active high-valent elements (Sn/Mn^{4+}/Ti/Zn/Mg) inhibit interlayer sliding and structural degradation; Light elements (e.g., B) widen sodium layer spacing to mitigate phase transition stress while enhancing structural rigidity

through strong covalent bonds [88, 100, 106, 107]. In addition, some other doping methods such as gradient doping establishes energy barriers at phase interfaces, forcing phase transitions to proceed via a quasi-solid-solution mechanism. Combined with the 3D steric hindrance network formed by P3/O3 dual-phase synergy, this mechanically restricts slip amplitude through interlocked stress fields. This achieves thermodynamic and kinetic synergy, maintaining reversible phase transition pathways and structural integrity during repeated Na^+ (de)intercalation.

The enhancement of interfacial stability primarily stems from the synergistic interplay between high-entropy strategies and structural regulation. On one hand, multi-element doping reinforces the rigidity of the lattice framework and optimizes electronic structures, suppressing lattice oxygen migration and irreversible redox reactions under high voltages, thereby reducing oxygen loss and electrolyte decomposition triggered by reactive oxygen. On the other hand, the disordered high-entropy configuration homogenizes electrochemical stress distribution and mitigates lattice volume fluctuations, inhibiting crack propagation and structural degradation. Concurrently, strengthened covalency in TM–O bonds and stabilized sodium-ion diffusion channels further suppress interfacial side reactions. Thermodynamic entropy maximization stabilizes and simplifies reversible phase transition pathways, ultimately enabling the formation of a dense, chemically compatible interface layer that minimizes electrolyte penetration and gas evolution risks [108].

The regulation of air stability is rooted in phase transition stability and interfacial stability. The disordered distribution of multiple elements reduces material surface activity, suppressing chemical corrosion reactions with atmospheric components and mitigating sodium ion loss and alkali compound formation. The entropy stabilization effect from the high-entropy configuration enhances lattice rigidity, alleviating the sensitivity of sodium layers to moisture or oxygen [109]. Simultaneously, inert element doping optimizes electron localization states, inhibiting

the enhanced covalency of TM–O bonds and structural distortion to stabilize interlayer charge distribution. Additionally, specific elements (e.g., Li and Al) expand interlayer spacing and create vacancy buffering mechanisms, weakening Na^+ shielding effects and enhancing oxidation resistance. This synergistically suppresses surface phase transitions and structural degradation, maintaining chemical inertness and structural integrity in ambient conditions [91, 110].

Indeed, the diversity of dopant elements enables high-entropy doping to simultaneously address multiple challenges (Table 2), whereas most experimental results also resist attribution to a single mechanism [111]. Based on the four major effects of high-entropy materials, the high-entropy strategy has accomplished multi-directional collaborative optimization of phase transition, interface, and air stability in LTMOs. Furthermore, the multi-element synergistic effect can fortify lattice covalent bonds, optimize sodium layer spacing and charge distribution, mitigate volume fluctuations during the intercalation and deintercalation of sodium ions, and enhance the material's oxidation resistance and chemical inertness [84, 89, 94]. Through this synergy, the high-entropy strategy has constructed a multi-directional stabilization mechanism of "thermodynamics–kinetics–chemical compatibility" for the layered oxide cathode materials of SIBs. This has led to a remarkable improvement in the overall performance of the materials, spanning from the micro-scale to the macro-structural level.

3 | High Entropy Prussian Blue Analogs

Although the high-entropy strategy has achieved significant performance improvements in the application of LTMOs, its structural stability remains limited by the Jahn–Teller effect. This limitation naturally motivates the exploration of PBAs with open-framework structures. The abundant vacancies within

TABLE 2 | Synergistic mechanisms of high-entropy effects in addressing key challenges for HE-LTMOs.

| Challenge type	Dominant high-entropy effects	Mechanism description
Phase transition stability	High-entropy effect, lattice distortion effect	Multi-element disorder increases configurational entropy, reducing phase transition driving force; ionic radius mismatch suppresses TM-layer sliding and irreversible O3–P3 transitions.
Interfacial stability	Cocktail effect, sluggish diffusion effect	Multi-element synergy enhances covalency of TM–O bonds, inhibiting lattice oxygen release; increased atomic diffusion barrier slows oxygen migration and electrolyte decomposition, promoting dense CEI formation.
Air stability	High-entropy effect, cocktail effect	High-entropy surface reduces chemical reactivity, suppressing Na^+/H^+ exchange; electronegative elements (e.g., Sn, Ti) strengthen TM–O bonds, mitigating water erosion and alkaline byproduct formation.
Oxygen loss	Cocktail effect, lattice distortion effect	Multi-element doping enhances electron localization around oxygen, raising oxygen migration barrier; lattice distortion constrains oxygen vacancy diffusion, suppressing sustained oxygen loss.
Na^+ diffusion kinetics	Lattice distortion effect, sluggish diffusion effect	Lattice distortion creates low-energy pathways for Na^+ migration; multi-element synergy reduces electrostatic potential in Na layers, enhancing ionic conductivity.

PBAs offer an ideal platform for incorporating high-entropy ions. However, the practical application of PBAs still encounters critical challenges: structural vacancies and the presence of crystalline water can lead to reduced cycling stability and low initial Coulombic efficiency. Notably, the "lattice distortion", "slow diffusion", and "entropy stabilization" effects—hallmarks of high-entropy strategies—have been demonstrated as effective approaches to mitigate these intrinsic drawbacks of PBA materials. This chapter provides a systematic review of the application and progress of high-entropy strategies in the design of PBAs, aiming to elucidate their synergistic optimization mechanisms.

3.1 | Infrastructure and Characteristics

Prussian Blue (PB, molecular formula $Na_xM [Fe (CN)_6]$, $x \leq 1$). As a mainstream cathode material for sodium-ion batteries, demonstrates high theoretical capacity and rapid sodium-ion migration characteristics due to its face-centered cubic open framework (alternating Fe/M-C $\equiv$ N-M′ arrangement), three-dimensional macro-porous structure, and low-cost synthesis advantages, making it an ideal candidate for large-scale energy storage applications [112]. However, limitations such as vacancy defects, crystalline water occupying effective sodium sites, and poor conductivity lead to low capacity and significant cycling degradation [113, 114]. Therefore, many researchers focus on Prussian Blue analogs (PBAs). The molecular formula of PBA cathode materials can be expressed as $A_xM_1 [M_2(CN)_6]_1$

$_{-y} \cdot \square_y \cdot nH_2O$ ($0 \leq x \leq 2$, $0 \leq y < 1$) (Figure 9a), where A is Na/K, M_1 and M_2 are different coordinated transition metal ions (M_1 coordinates with N, M_2 with C), such as Mn, Fe, Co, Ni, Cu, Zn, Cr, etc. $\square$ represents $[M_2(CN)_6]$ vacancies [115]. In $A_xM_1M_2(CN)_6$, materials with $x \leq 1$ are termed sodium-deficient states (Prussian Blue, PB), whereas those with $x > 1$ are sodium-rich states (Prussian White, PW) [116]. PBAs can regulate redox potentials and enhance capacity by introducing different transition metals at M_1 or M_2 sites. PW exhibits both high capacity and low-stress structural advantages due to occupancy of interstitial sodium ions and single metal valence states (e.g., Fe^{2+}/Fe^{3+}) [116].

The mainstream synthesis of PBAs for sodium-ion batteries involves coprecipitation reactions between $Na_4Fe [CN]_6$ and transition metal ions. However, this process inevitably introduces intrinsic defects such as vacancies of Fe $[CN]_6$, coordinated water, and interstitial water (Figure 9b), leading to incomplete crystal structures and severely degraded electrochemical performance. Specifically, Fe $[CN]_6$ vacancies disrupt the Fe–CN–TM bridging structure, not only reducing redox-active sites but also inducing lattice distortion to form sodium-deficient cubic phases. The breakage of electron conduction paths caused by vacancies further decreases material electronic conductivity, exacerbating electrode polarization effects. Additionally, vacancies compromise lattice integrity, causing severe lattice distortion or even structural collapse during Na^+ extraction/insertion, resulting in significant cycling degradation [117]. Current research suggests that interstitial water reduces the specific capacity of PBAs, whereas stable
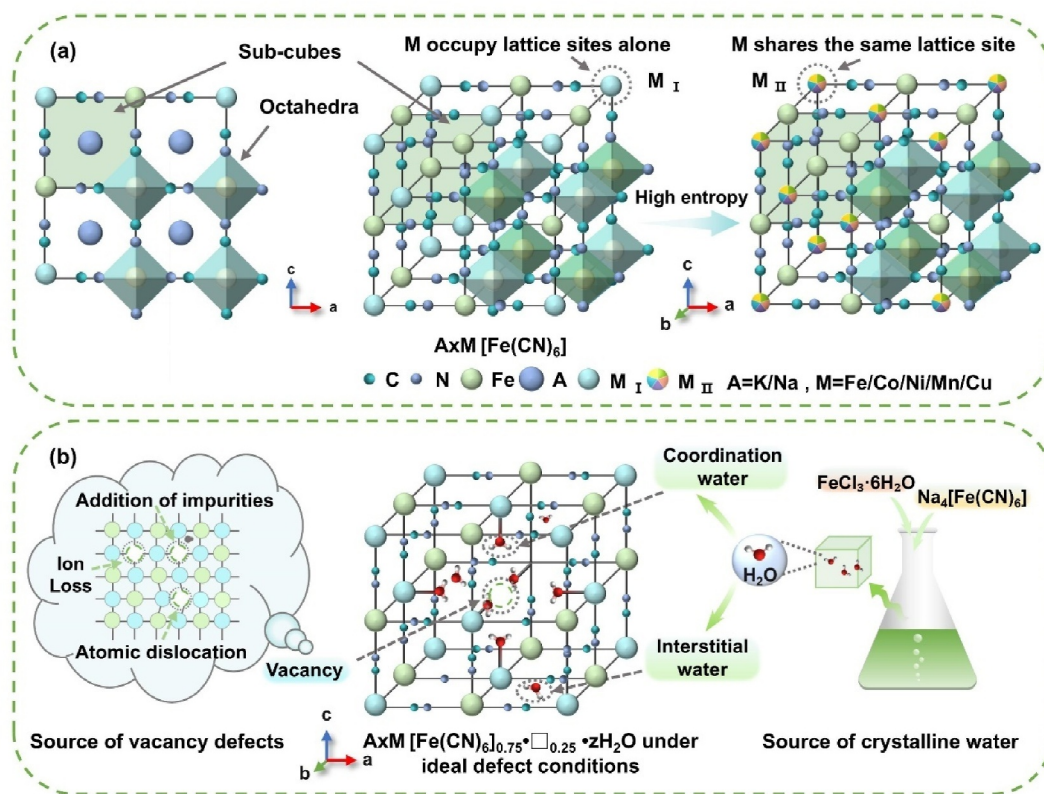
FIGURE 9 | (a) Basic structural framework of PBAs ($A_xM [Fe [CN]_6$ as an example). (b) Vacancy defects and crystallization water problems of PBAs ($A_xM [Fe [CN]_6]_{0.75} \cdot \square_{0.25} \cdot _zH_2O$ as an example).

coordinated water improves cycling life [118]. Specifically, unstable interstitial water occupies ion storage sites, hinders Na^+ migration, participates in side reactions, reduces conductivity, and severely impacts capacity and cycling performance [119]. When interstitial water desorbs into the electrolyte, hydrolysis side reactions occur, reducing specific capacity and potentially causing gas evolution, posing serious safety risks [120]. In contrast, small amounts of coordinated water can replace conjugated structures in vacancies, playing a critical role in stabilizing the lattice [118, 121]. Beyond crystallinity and water-related issues, high-spin Fe^{2+} in PBAs is highly susceptible to oxidation into low-spin Fe^{3+} during synthesis, repelling Na^+ ions and forming extensive sodium-deficient phases, leading to severe structural changes [122, 123].

3.2 | High Entropy Strategy and Application

The above-mentioned problems have been modified by PBAs through morphological regulation, material composite, surface coating, element substitution or doping, etc. in previous studies, and positive progress has been made [124–126]. However, their practical applications remain limited by problems such as Fe $(CN)_6$ vacancy defects, capacity decay caused by lattice water molecules, and insufficient cycling performance. In contrast, high-entropy strategies introduce multi-metal co-doping, structural regulation and defect engineering, as well as entropy stabilization, providing new approaches to tackle these challenges.

### 3.2.1 | Polymetallic Doping Strategies

Polymetallic doping forms a high-entropy system by introducing multiple elements (not limited to transition metals). Through the high-entropy effect, it reduces the water content and vacancy defects in the PBA framework, optimizes the local coordination environment and electronic structure, and inhibits material phase transformation and structural degradation, significantly enhancing the electrochemical activity and structural stability of PBAs. Specific metal elements maintain similar functional roles across different systems. In the K-doped high-entropy PBA system K_x (MnFeCoNiCu) [Fe $(CN)_6$] (HE-K-PBA), Mn, Fe, Co, and Cu serve as active elements for charge compensation, whereas Ni functions as an inactive element stabilizing the structural framework. K^+ substitution not only partially replaces Na^+ to enable permanent (de)intercalation but also elevates the working voltage to 3.46 V through its lower redox potential (Figure 10a), resulting in enhanced energy density. The high-entropy strategy ensures uniform distribution of five transition metal elements at nitrogen-coordinated sites, forming a stable framework that effectively mitigates structural distortion during charge/discharge cycles. This optimized configuration achieves improved sodium ion diffusion coefficients (D_{Na}^+) (Figure 10b) and enhanced sodium storage kinetics (Figure 10c), leading to exceptional long-term cycling stability [127]. Similarly, in Ni-PBAs, the introduction of Fe, Co, Mn, and Cu active elements replaces electrochemically inert Ni sites, facilitating reversible Na^+ (de)intercalation (Figure 10f)

and thereby increasing specific capacity (Figure 10d). This modification also promotes electron transfer and rapid charge compensation. The three-dimensional energy level hybridization effect elevates valence electron concentration, activating multiple redox centers (Figure 10e). Thermogravimetric analysis (TGA) reveals that HE-PBA ($Na_{1.36}Ni_{0.4}Fe_{0.15}$-$Co_{0.15}Mn_{0.15}Cu_{0.15}$ [Fe$(CN)_6$]) exhibits lower weight loss than Ni-PBA above 270°C, indicating that multi-metal cation incorporation effectively reduces crystal vacancies and enhances thermal stability [61]. Furthermore, the equimolar five-component high-entropy system M_5HCF (Na_2(MnCoNi-CuZn)$_{0.2}$ [Fe$(CN)_6$]) demonstrates improved performance through metal d-orbital hybridization, which narrows the band gap and facilitates electron excitation to the conduction band (Figure 10g,h). Concurrently, high-entropy doping reduces water content in PBAs and regulates spin states to mitigate Jahn–Teller distortion. These combined mechanisms endow HE-PBA with superior cycling stability and rate capability compared to conventional Ni-PBAs [128].

3.2.2 | Structural/Defect Engineering Strategies

Beyond compositional regulation through elements, structural optimization, and defect engineering are also key to enhancing the performance of PBAs. In conjunction with the high-entropy strategy, approaches such as morphology control, single-crystallization, and structural fusion can be employed to further optimize sodium-ion transport pathways and structural integrity. With the assistance of high-entropy strategy, structural regulation and defect engineering significantly enhance the sodium storage kinetics and stability of PBAs by optimizing the microstructure and defect distribution of materials. The combination of high-entropy structure and unique morphology can enhance the performance improvement brought by structural engineering. For instance, the combination of single-crystal and high-entropy strategies can effectively suppress lattice distortion and transition metal dissolution. The single-crystal strategy significantly reduces the vacancies and water content in the material (Figure 11a), forming a high-sodium-content monoclinic phase. The complete framework structure increases the thermal decomposition temperature of SC-HEPBA and improves thermal stability (Figure 11b). The high-entropy and defect-suppressing structure enables unrestricted Na^+ diffusion, and in coordination with the single-crystal strategy, SC-HEPBA achieves reversible monoclinic–cubic–-tetragonal phase transitions with small volume changes, significantly inhibiting metal dissolution and improving structural integrity, thereby enhancing cycling stability [129].

When the high-entropy strategy is combined with the hollow stepped spherical morphology of PBAs, it not only increases the surface area for Na^+ diffusion but also significantly shortens the average diffusion distance of Na^+ (Figure 11c), thereby improving Na^+ diffusion kinetics (Figure 11d). Through the disordered distribution of multiple metals and the hollow stepped spherical structure, the volume change is effectively mitigated, achieving a high-rate performance of 76.4 mAh g^{-1} at 4.0 A g^{-1} and a capacity retention rate of 75.6% after 1000 cycles
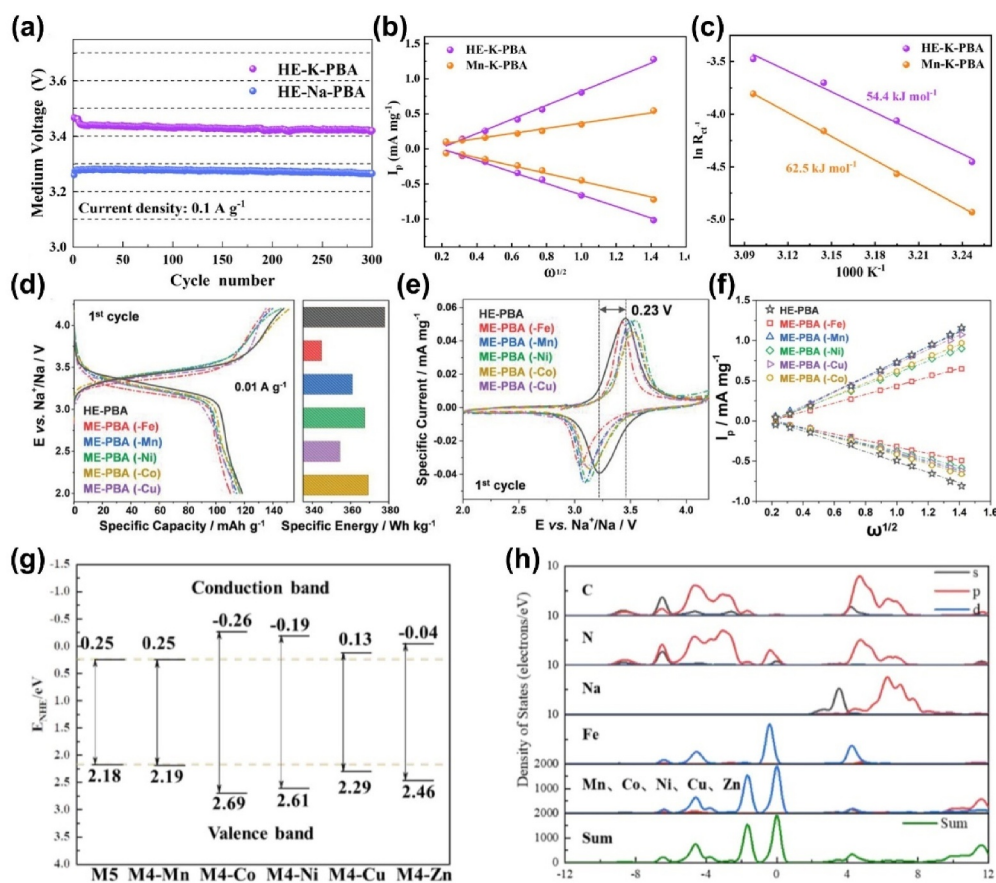
FIGURE 10 | (a) Long-term median voltage performance of HE-K-PBA and HE-Na-PBA at 0.1 A g^{-1}. Reproduced with permission [127]. Copyright 2023 American Chemical Society. (b) Linear fitting Randles-Sevcik curves of HE-K-PBA and Mn-K-PBA by plotting the maximal current as a function of the square root of the sweep rate. Reproduced with permission [127]. Copyright 2023 American Chemical Society. (c) Arrhenius plots and corresponding activation energy of HE-K-PBA and Mn-K-PBA. Reproduced with permission [127]. Copyright 2023 American Chemical Society. (d) First-cycle voltage profiles at 0.01 A g^{-1} (left) and comparison of specific energies (right). Reproduced with permission [61]. Copyright 2021 Wiley. (e) Initial cyclic voltammogram at 0.05 mV s^{-1} for HE-PBA and the different ME-PBAs. Reproduced with permission [61]. Copyright 2021 Wiley. (f) The linear response of specific peak current as function of the square root of the sweep rate for determining the apparent sodium-ion diffusion coefficient. Reproduced with permission [61]. Copyright 2021 Wiley. (g) Schematic diagram of the band edges for M$_5$HCF and medium entropy doped PBAs. Reproduced with permission [128]. Copyright 2023 Royal Society of Chemistry. (h) DOS and PDOS plots of M$_5$HCF. Reproduced with permission [128]. Copyright 2023 Royal Society of Chemistry.

[130]. Furthermore, the high-entropy strategy can also assist in the combination of different structures to achieve complementary advantages. The traditional double octahedral connection structure (DOC) in Prussian blue is limited by its insufficient structural stability and narrow ion transport channels, which restricts the cycling and rate performance of the material. The tetrahedral–octahedral (TOC) structure exhibits higher structural stability and ion transport capability, but is limited by electrochemically inert elements such as zinc, resulting in low capacity. However, the difference in configuration and formation speed between the two structures makes it difficult to achieve uniform fusion. The use of double polymerization reactions combined with the high-entropy strategy can achieve uniform fusion of DOC and TOC, optimizing central metal coordination environment (Figure 11e,f), enhancing the structural stability through the enhancement of C ≡ N bond (Figure 11g), and significantly enhancing the electrochemical performance of PBAs. Compared with the single-structured DOC materials, the TOC/DOC fused structure (HE-Zn/PPy) demonstrates a more robust structure, a larger ion diffusion channel, and better cycle and rate performance [131].

3.2.3 | Entropy Increases Stability Strategies

The entropy increase stabilization mechanism can significantly enhance the structural stability and electrochemical cycling stability of PBAs by rationally regulating the configurational entropy and taking advantage of the intrinsic connection between configurational entropy/disorder degree of components and the cycling stability of PBAs materials. The HEM-HCF introduces five equimolar metals into the PBA lattice, resulting in a configurational entropy $\Delta S_{\text{config}} = 1.61$ R, inducing lattice distortion and a "pinning effect" that suppresses the cell volume change during sodium intercalation and deintercalation to below 0.6%, significantly improving the cycling stability compared to single-metal systems.
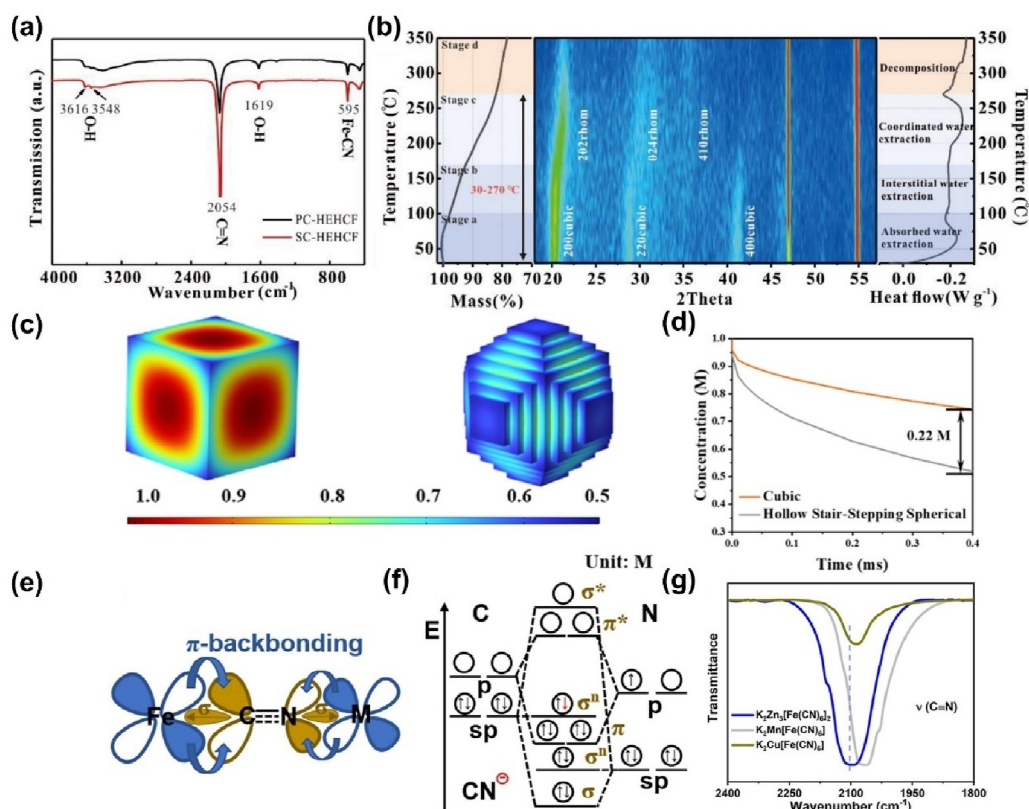
FIGURE 11 | (a) FTIR curves of PC-HEHCF and SC-HEHCF. Reproduced with permission [129]. Copyright 2023 Elsevier. (b) SC-HEPBA structural evolutions during heating from 30°C to 350°C, corresponding TGA and DSC curves are shown at the left and right. Reproduced with permission [129]. Copyright 2023 Elsevier. (c) Distributions of Na$^+$ surface concentration by COMSOL Multiphysics simulation and (d) curves of the Na$^+$ concentration inside the cubic and hollow stair-stepping spherical models after diffusing of 0.4 ms. Reproduced with permission [130]. Copyright 2024 American Chemical Society. (e) Representation of metal-N≡C interaction by σ bonding and π-back bonding. Reproduced with permission [131]. Copyright 2025 Elsevier. (f) Molecular orbital diagram for C≡ N ligand. Reproduced with permission [131]. Copyright 2025 Elsevier. (g) FTIR spectra of three single-metal hexacyanoferrates. Reproduced with permission [131]. Copyright 2025 Elsevier.

The high-entropy effect, by reducing the atomic diffusion coefficient and increasing the activation energy for phase separation, shows significant advantages in cycling stability, Coulombic efficiency, and rate performance [132]. The increase in entropy can also exhibit quasi-zero-strain behavior during the charge-discharge process. The HE-HCF with a disordered Rubik's cube structure reduces the Gibbs free energy through the entropy increase effect, demonstrating an ultra-long cycle life of over 50,000 cycles and an excellent fast-charging capability up to 75C. The best sample remains structurally unchanged after being exposed to air for 3 months (Figure 12a), breaking the air stability limit of traditional materials. Specifically, the high-entropy strategy enhances the bond strength (ICOHP value increases, Figure 12b), inhibits the Jahn–Teller effect of Mn. Meanwhile, the sodium ion diffusion remains isotropic, and the activation energy decreases (Figure 12c), improving the kinetic performance. Additionally, the increased entropy in HE-HCF not only enhances structural stability and thermal/air stability, but also enables a highly reversible zero-strain two-phase Na$^+$ storage mechanism, reducing the migration energy barrier of Na$^+$ [133]. With the increase in entropy, materials tend to form high-symmetry structures during electrochemical cycling. The high-entropy strategy-introduced Prussian white (HE-PW) significantly improves the structural stability of PW by suppressing structural phase transitions and gas generation during Na$^+$ insertion/

extraction. On one hand, the disordered distribution of multiple metals inhibits the transformation from monoclinic to tetragonal phase. Systems with lower component disorder are more prone to phase transitions, while the entropy increase of HE-PW significantly reduces the phase transition driving force, maintaining a high-symmetry structure during cycling and raising the phase transition energy barrier to 1.8 eV, thereby blocking harmful phase transition pathways. On the other hand, the entropy increase suppresses the undesirable evolution of gases during cycling (Figure 12d), resulting in nearly zero-strain lattice parameter changes during charging and discharging, and a capacity retention rate of over 90% after 200 cycles [134].

3.3 | Performance Improvement Mechanism

The high-entropy strategy systematically addresses core challenges of PBAs in sodium-ion batteries (capacity decay, irreversible phase transitions, and sluggish kinetics) through multi-component synergy, structural optimization, and thermodynamic stabilization. The intrinsic mechanisms of performance enhancement can be analyzed from four dimensions:

High-entropy systems introduce diverse transition metals to create local coordination environment heterogeneity, breaking
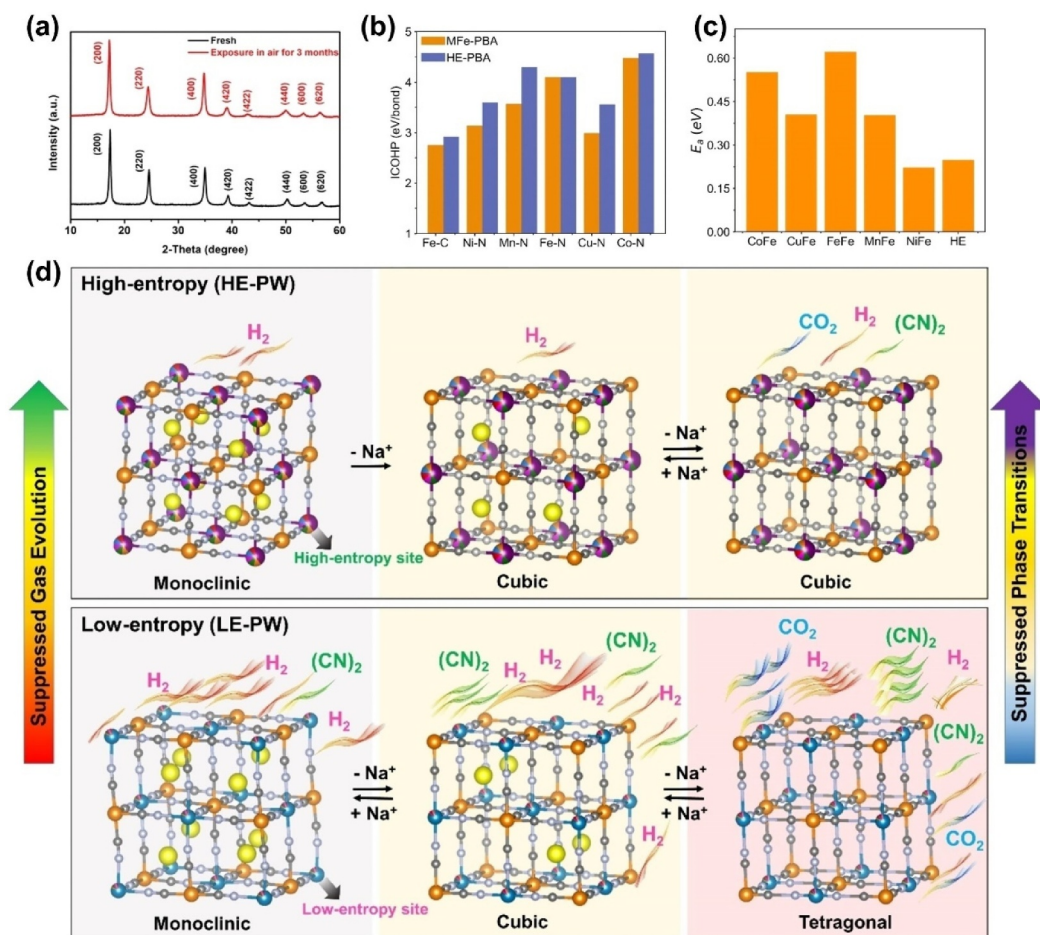
FIGURE 12 | (a) XRD comparison of the HE-HCF powder in the fresh state and after exposure to air for 3 months. Reproduced with permission [133]. Copyright 2023 Wiley. (b) The integrated crystal orbital Hamilton population values of various bonds. Reproduced with permission [133]. Copyright 2023 Wiley. (c) The diffusion activation energies of MFe-HCF and HE-HCF in cubic phase. Reproduced with permission [133]. Copyright 2023 Wiley. (d) Schematic illustration of the structural evolutions and corresponding gassing behavior of HE-PW and LE-PW. Reproduced with permission [134]. Copyright 2024 Wiley.

the electronic structure limitations of single-metal PBAs. Hybridization of multiple d-orbitals narrows the material's bandgap, reducing the energy barrier for electron transitions from valence to conduction bands, thereby improving electron mobility [128]. Simultaneously, multi-metal synergy activates multiple redox centers, broadening the redox potential window and ensuring reversible Na^+ insertion/extraction across wider voltage ranges. Additionally, intermetallic charge compensation suppresses oxidation tendencies of high-spin metals, mitigating Jahn–Teller distortions induced by spin-state transitions to maintain lattice integrity [130, 132].

High-entropy design promotes atomic-level homogeneous doping through entropy-driven effects, significantly reducing the formation of $Fe(CN)_6$ vacancy defects. The decreased vacancy density not only maintains structural continuity to ensure unimpeded electron conduction pathways but also prevents lattice distortion caused by localized stress concentration during Na^+ (de)intercalation [48]. Furthermore, combining high-entropy strategies with single-crystallization or morphological engineering optimizes material microstructure. The integrity of single-crystal frameworks eliminates grain boundary obstruction to ion migration, whereas rational morphology control provides

short-range diffusion pathways for Na^+, lowering diffusion energy barriers and enabling rapid stable ion transport [130].

The high configurational entropy of high-entropy systems significantly enhances thermodynamic stability. During Na^+ (de)intercalation, the "atomic-scale pinning effect" from multi-component disorder inhibits abrupt lattice parameter changes and reduces driving forces for irreversible phase transitions, enabling near-zero strain behavior [132]. Entropy effects also compensate for Gibbs free energy increases caused by Na vacancy formation, maintaining low-energy states even in highly sodiated structures. Additionally, multi-metal synergy weakens the binding energy between Fe^{3+} and coordinated water, suppressing interstitial water desorption and electrolyte decomposition side reactions, thereby improving cycling stability [128].

The high-entropy strategy achieves performance optimization from atomic to mesoscopic scales through the synergy of multi-metal doping, defect engineering, and structural regulation. At the atomic scale, multi-component disorder enhances lattice rigidity to suppress phase transitions; at the nanoscale, single-crystallization or hierarchical pores optimize ion transport pathways; at the macroscopic scale, entropy stabilization lowers

TABLE 3 | Synergistic mechanisms of high-entropy effects in addressing key challenges for HE-PBAs.

Challenge type	Dominant high-entropy effects	Mechanism description
Vacancy defect suppression	High-entropy effect, lattice distortion effect	Uniform multi-element doping reduces Fe $(CN)_6$ vacancy formation; lattice distortion induces a "pinning effect," inhibiting vacancy aggregation and structural collapse.
Crystalline water control	High-entropy effect, cocktail effect	High-entropy composition lowers surface energy, reducing water adsorption; strongly coordinating elements (e.g., Zn and Ni) replace partial Fe sites, decreasing crystalline water content and stabilizing coordinated water.
Phase transition reversibility	Sluggish diffusion effect, high-entropy effect	Multi-atomic diffusion barrier delays structural rearrangement; high configurational entropy stabilizes the cubic phase, suppressing detrimental monoclinic-tetragonal transitions.
Cycling stability	Cocktail effect, lattice distortion effect	Hybridization of multiple metal d-orbitals enhances electron conduction; lattice distortion homogenizes stress distribution, enabling near-zero-strain Na^+ (de)intercalation.
Oxidation state control	Cocktail effect, high-entropy effect	Inter-element charge compensation inhibits excessive Fe^{3+} oxidation, maintaining low-spin state; high-entropy environment stabilizes local coordination fields, mitigating Jahn–Teller distortion.

the system's overall energy state. This cross-scale synergy maintains stable Na storage sites, rapid reaction kinetics, and mechanical stress mitigation during cycling, collectively overcoming the comprehensive performance limitations of conventional PBAs (Table 3).

4 | Challenges and Optimization Direction

HE-LTMOs and HE-PBAs represent emerging strategies for sodium-ion battery cathodes. Leveraging the structural stability and superior electrochemical performance derived from their high configurational entropy effect, they exhibit significant application potential. However, research on high-entropy battery materials remains in its early stages, and their practical application faces critical challenges including the complexity of multi-element systems, limitations of synthesis processes, inadequacies in characterization techniques, and ambiguity in structure-property mechanisms. Future research should address these challenges by focusing on four key dimensions: rational design of high-entropy systems, innovative synthesis processes, optimized characterization methods, and in-depth mechanistic analysis.

4.1 | Rational Design of High-Entropy Systems

In designing high-entropy material systems, although multiple elements can suppress phase separation and enhance structural stability via the high-entropy effect, the sensitivity of layered oxides to element valence states and site occupancy leads to local structural distortion, element segregation, and inactive phase formation when mismatches in ionic radius, electronegativity, or redox activity occur. This consequently deteriorates sodium-ion diffusion kinetics and specific capacity [87, 135]. Simultaneously, the lack of universal rules for element functionalization (e.g., charge compensation, glide suppression, and oxygen anchoring) further increases the cost of material design.

Although the high-entropy strategy demonstrates significant potential in enhancing the performance of electrode materials, it still faces several inherent challenges and limitations on the path to practical application, which require careful consideration during material design. For instance:

Performance-wise: The different cations introduced into a high-entropy system typically play distinct functional roles during reactions, such as conductive, active, and structural roles. This inevitably includes components that are electrochemically inert or exhibit low activity. Although these components may contribute to structural stabilization, they dilute the overall concentration of redox-active sites, potentially leading to a lower specific capacity compared to traditional binary or ternary cathode materials [136]. Future designs need to more precisely balance the ratios of different functional elements or explore highly active multi-principal element combinations with multi-electron reactions to mitigate this capacity dilution effect.

Synthesis-wise: The homogeneous synthesis of high-entropy materials heavily relies on the precise stoichiometry and atomic-level uniform mixing of multiple high-purity metal precursors. This presents significant challenges, including the difficulty in controlling precursor consistency, complex synthesis processes, and substantial cost increases. For example, to ensure the formation of a homogeneous solid solution rather than impurity phases during solid-state diffusion, higher sintering temperatures, longer heat treatment times, or more complex processes are often required [137]. This is a key area requiring prospective consideration during the design of future high-entropy materials, especially in the context of commercialization.

Characterization-wise: The increased number of element types in high-entropy systems necessitates more diverse and refined characterization techniques, particularly for accurately characterizing and resolving the random distribution, local coordination environments, and possible short-range order of multiple elements at the sub-nanometer scale [138]. Furthermore, the

structure–property relationships become more complex. Any minor modification or adjustment of a single element may amplify its impact on the overall performance through synergistic effects, posing a significant challenge for the rational design of material systems and the trade-off of properties.

In future systematic design strategies based on ionic radius gradients, electronegativity matching, and charge compensation capability, quantitative descriptors such as cationic potential can be further incorporated to provide a rational design basis for the precise construction of high-entropy systems [139]. On one hand, controlling the difference in ionic radii of transition-metal ions within a specific threshold helps reduce lattice stress. On the other hand, balancing the redox activity among elements avoids competitive reactions that would disrupt the host framework, thereby advancing the paradigm of materials design from "trial-and-error" toward quantitative design [140].

4.2 | Innovative Synthesis Processes

The synthesis processes for high-entropy materials mainly include solid-phase methods and liquid-phase methods. Among them, solid-phase methods are the mainstream path for scaled-up production, encompassing traditional ball milling, high-pressure/high-temperature methods, and emerging rapid Joule heating techniques. Liquid-phase methods, favored for laboratory-scale synthesis, enable better atomic-level mixing and precise morphology control, and include sol-gel, co-precipitation, and solvothermal methods. Furthermore, some emerging synthesis methods with unique advantages have been developed for high-entropy materials [136].

When synthesizing HE-LTMOs, solid-phase methods offer advantages such as simple processes and ease of industrialization, making them suitable for thermodynamically stable phases. However, they rely on bulk diffusion at high temperatures, making it difficult to achieve uniform mixing of multiple cations at the atomic scale, which can easily lead to local compositional segregation and affect material purity. Moreover, prolonged high-temperature annealing can exacerbate sodium loss and disproportionation reactions of transition metals, causing oxidation state fluctuations and impurity phase formation. Compared to solid-phase methods, the sol-gel method forms uniform nanoparticle gels through hydrolysis and condensation. Its advantage lies in mixing precursors at the molecular scale in solution, providing an ideal starting point for achieving atomic-level homogeneity and enabling precise control over stoichiometry. However, the sol-gel process has a long cycle time, and differences in the hydrolysis or polycondensation rates of precursors can easily lead to agglomeration, especially during scale-up. Additionally, although the solvothermal method can achieve morphology control and accelerate ion diffusion by adjusting process parameters, it suffers from low yield and is likely to introduce intergranular lattice discontinuities and surface residual alkali.

For the synthesis of HE-PBAs, the common co-precipitation method involves reacting multi-metal ion solutions with a precipitating agent to obtain uniformly composed precursors, which are then calcined at high temperature to obtain the target product. However, process parameters such as concentration, temperature, pH, and time during synthesis significantly affect the product and are difficult to control precisely. Therefore, overcoming the limitations of traditional co-precipitation requires a focus on developing precisely controlled multi-element co-precipitation techniques. On one hand, dual-injection pumps or multi-channel feeding systems can be employed to precisely control the feed rates and mixing sequences of different metal salt solutions, enabling efficient co-precipitation rather than layered precipitation. On the other hand, introducing chelating agents (such as sodium citrate or EDTA) can form complexes with different metal ions, each with varying stability constants, thereby balancing their solubility product differences, stabilizing the metal ions, promoting synchronous nucleation, and improving product quality and synthesis efficiency. Furthermore, by precisely regulating the local pH, temperature, and stirring intensity within the reactor, a uniform nucleation and growth environment can be created, effectively inhibiting compositional segregation and crystal defects [141, 142]. Building on this, further strategies such as ligand environment design, reaction kinetics optimization, or gradient synthesis can achieve synchronous nucleation and uniform growth of multivalent precursors. Concurrently, developing anhydrous or low-water-content synthesis systems, combined with post-treatment techniques to reduce crystalline water content in the material, helps reconstruct the structural continuity of sodium-ion transport channels and enhance electrochemical performance.

Furthermore, for both HE-LTMOs and HE-PBAs, optimizing the synthesis process requires attention to emerging methods that offer advantages such as high efficiency, homogenization, and intelligence. For example, microwave-assisted synthesis enables ultrafast energy transfer through molecular-level selective heating, significantly shortening reaction time while suppressing sodium volatilization and grain coarsening [143]. The spatial confinement oxidation strategy can load high-entropy oxides onto single-walled carbon nanotube (SWCNT) surfaces, restricting grain growth and enhancing conductivity through confinement effects, thereby reducing interfacial resistance and achieving uniform element distribution [144]. Spray pyrolysis atomizes multi-metal precursor solutions into micro-droplets, enabling instantaneous drying, decomposition, and reaction in a high-temperature reactor. This method allows for the one-step synthesis of compositionally uniform nano- or sub-micron spherical particles and is easily adaptable to continuous production, providing an efficient pathway for the controlled preparation of high-entropy materials [145]. Electrospinning involves spinning a mixture of multi-metal precursors with high-molecular-weight polymers, followed by heat treatment, to obtain flexible, self-supporting high-entropy electrode materials featuring a continuous conductive network, high specific surface area, and short ion diffusion paths [146].

4.3 | Optimization of Characterization Methods

The lack of advanced characterization techniques severely constrains the analysis of microscopic mechanisms. Because of

insufficient spatial resolution and dynamic response capabilities, conventional tools such as XRD and SEM fail to accurately track multi-element distribution, atomic site preference, and hierarchical structural evolution. Even with sophisticated instruments, characterizing atomic-scale features (e.g., lattice distortion and local ordered configurations) still faces technical bottlenecks [80, 147]. Therefore, it is necessary to optimize the integration of multimodal techniques, such as in situ XRD, TEM, and XANES, to track in real-time the lattice distortion, phase transition pathways, and dynamic valence state responses of transition metals during sodium (de)intercalation. Additionally, priority should be given to combining aberration-corrected HAADF–STEM with EELS atomic-scale imaging to precisely resolve transition metal layer site preferences, oxygen vacancy distribution patterns, and their coupling relationships with sodium interlayer spacing [148].

4.4 | Deepening Mechanistic Analysis

The interpretation of structure-property relationships remains challenging due to the highly coupled nature of multi-element synergistic effects, making it difficult to isolate the influence of individual variables. In addition, methods for in situ tracking of the cross-scale kinetic evolution bridging the microscopic atomic environment and macroscopic phase transformations are lacking. The complex interplay between thermodynamics and kinetics is also difficult to decouple [53, 149]. Furthermore, insufficient spatiotemporal resolution in *in situ* characterization (e.g., dynamic capture of microcrack propagation and oxygen loss pathways) and challenges in integrating multimodal data further impede the quantitative correlation of "composition–structure–performance". These interconnected challenges collectively limit breakthroughs in the practical application of HE-LTMOs in high-performance sodium-ion batteries.

However, gaining deeper insights into high-entropy mechanisms requires advances in fundamental experimental research, characterization methods, and computational tools. Future work should integrate multi-scale in situ characterization with machine learning-assisted molecular dynamics simulations and high-throughput calculations. This integration aims to dynamically track entropy-dominated energy barrier changes along sodium-ion diffusion pathways, resolve the influence of multi-element valence states on oxygen framework stability, and establish a cross-scale theoretical model for "electron–ion–lattice" transport [150]. Ultimately, this will provide profound insights into the structure–property mechanism of high-entropy configurations.

4.5 | Commercial Viability and Environmental Friendliness

When developing high-entropy cathode materials in the future, enhancing commercially viable attributes and meeting environmentally friendly requirements are also critical directions to consider. For commercialization, prioritizing the development of cathode materials exhibiting high energy density and long cycle life over a wide voltage range is essential [148].

Concurrently, good rate capability is fundamental for enabling fast charging in current new energy vehicles, whereas applicability across a broad temperature range (particularly low-temperature performance) is a crucial performance requirement for expanding application scenarios. Furthermore, designing high-entropy systems solely for extreme performance without considering cost-effectiveness is detrimental to commercial application. Substituting elements with similar functionalities (e.g., Fe/Mn for Co/Ni) offers a potential route to cost reduction [101]. It is important to note that while incorporating multiple elements in high-entropy cathodes enhances performance, it simultaneously introduces new challenges for recycling processes and environmental friendliness. This necessitates a comprehensive life-cycle consideration, ranging from designing with non-toxic elements to optimizing recycling procedures.

4.6 | AI Empowerment

Artificial intelligence (AI) and machine learning (ML) technologies are profoundly transforming the research and development paradigm for HEMs. By constructing intelligent systems that span the entire chain of design, synthesis, and mechanism analysis, they accelerate the transition from empirical exploration to rational design, thereby driving their R&D and commercialization processes [151].

In terms of element combination design, machine learning models (such as random forest, support vector machines, or graph neural networks) can efficiently predict the probability of forming stable single-phase solid solutions for any proposed multi-element combination by learning from high-quality datasets generated by first-principles calculations (e.g., formation energies and crystal structure information). This enables rapid screening of promising high-entropy candidate materials within the vast compositional space. For example, Liu et al. demonstrated the effectiveness and advantages of AI in predicting the phase stability of multi-element combinations by training a deep neural network (DNN) as a surrogate model for CALPHAD calculations. This work, utilizing large-scale datasets, proved that DNNs could accurately predict phase fractions, including the BCC phase, and, after training on data from low-component systems, reliably predict the stable phase composition of multi-component alloy [152].

At the synthesis level, for a given target composition, AI can analyze the "synthesis conditions-product structure" correlation data extracted from literature and experimental databases. By training generative models or employing Bayesian optimization strategies, it can recommend optimal synthesis parameters for achieving high phase purity and uniform element distribution, significantly reducing experimental trial and error. For instance, Jaemin Wang et al. developed a hybrid AI model integrating convolutional neural networks and graph neural networks to explore the compositional space of high-entropy alloys. By simultaneously characterizing atomic-scale local environments and global compositional distributions, the model achieved high-precision classification of alloy phase structures and quantitative prediction of mechanical properties. Based on this,

the researchers employed inverse design using the recommended synthesis conditions to fabricate a novel Co/Cr/Fe/Ni/Mn-based high-entropy alloy, greatly enhancing synthesis efficiency. Experimental verification showed that this alloy achieved an excellent combination of strength and ductility, with a room-temperature tensile strength reaching 1.5 GPa, representing an approximate 40% improvement over conventional systems [153].

Furthermore, deep learning-based algorithms can efficiently parse large volumes of complex characterization data (e.g., XRD and XAS) and mine hidden "composition-structure-property" correlations within vast performance datasets, thereby guiding the inverse design and performance optimization of materials. Li et al. proposed deploying "Agentic AI" at synchrotron facilities to construct an autonomous characterization system centered on automation and the collaboration of specialized agents, forming a closed loop from experimental design and execution to multimodal analysis and reporting, accelerating material characterization and scientific discovery [154]. Ghose et al. developed a framework based on neural network ensembles and uncertainty quantification (UQ) for predicting molecular x-ray absorption spectra (XAS) while simultaneously providing prediction confidence intervals [155]. This method not only significantly improves the accuracy of spectral interpretation but also enhances the model's robustness against compositional and structural perturbations through its uncertainty output, providing an intelligent and interpretable analysis tool for extracting reliable structure-property relationships from complex spectroscopic data. Therefore, AI empowerment,

which integrates "candidate composition generation–synthesis scheme recommendation–experimental data parsing–feedback for optimized design" into an intelligent closed loop, is becoming a key driver in advancing high-entropy materials R&D [156–159].

5 | Conclusion and Outlook

As an innovative material design paradigm that transcends the traditional doping concept, the high-entropy strategy has profoundly transformed the research and development pathways for sodium-ion battery cathode materials. Its core lies in deliberately introducing multiple principal elements to construct high configurational entropy within the material, thereby triggering a series of synergistic "high-entropy effects" that systematically reshape the material's intrinsic properties across multiple dimensions, including thermodynamics, kinetics, and electronic structure. These four effects—the thermodynamically driven "High-entropy effect," the pronounced "Lattice distortion effect" caused by atomic size differences, the "Sluggish diffusion effect" that influences ion migration, and the "Cocktail effect" stemming from multi-element electronic interactions—collectively form the cornerstone for the performance leap in both HE-LTMOs and HE-PBAs (Figure 13).

In different cathode systems, the dominant roles and manifestations of these effects are context-dependent, revealing rich scientific implications and engineering value. In LTMOs, the
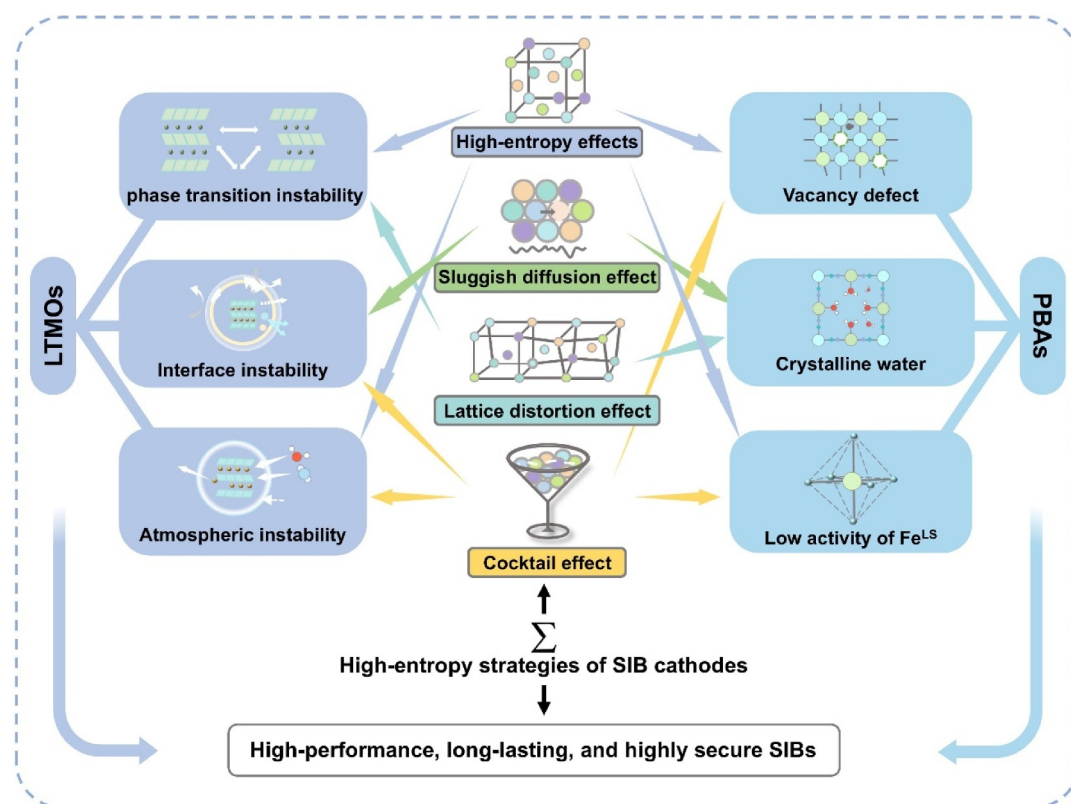
FIGURE 13 | Entropy-driven design unlocks high-performance SIB cathodes.

"High-entropy effect" fundamentally suppresses the thermodynamic driving force for harmful, complex phase transitions during high-voltage, deep desodiation by lowering the system's free energy, laying the foundation for structural reversibility [160]. The intense "Lattice distortion effect" acts like countless microscopic "rivets," effectively pinning the overall sliding of transition metal layers through introduced, continuous local stress fields, thereby mitigating accumulated strain during cycling. Concurrently, the "Sluggish diffusion effect" moderately adjusts the migration energy barrier for sodium ions, helping maintain a more uniform concentration gradient during rapid (de)intercalation and reducing local overloading. Meanwhile, the "Cocktail effect," through charge transfer and orbital hybridization among multiple metals, synergistically optimizes electronic conductivity and stabilizes lattice oxygen. Together, these effects achieve long-cycle stability under high voltage, enhanced air stability, and reduced voltage decay.

For PBAs, their open-framework structure provides a unique stage for high-entropy effects. The powerful "High-entropy effect" and "Lattice distortion effect" jointly enhance the rigidity of the three-dimensional framework, effectively resisting the lattice breathing stress induced by repeated sodium-ion insertion/extraction, and significantly reducing intrinsic defects and phase transition tendencies caused by [Fe(CN)$_6$] vacancies and crystalline water. The "Sluggish diffusion effect" in this system may manifest as a subtle modulation of sodium-ion migration paths within the broad channels, while the "Cocktail effect" optimizes the material's redox potential and electron conduction network through electronic synergy among different metal sites. These work in concert to achieve excellent rate capability, high cycling life, and higher electrode compaction density.

In contrast, polyanionic compounds (such as phosphates, fluorophosphates, and NASICON-type materials), as another pillar of sodium-ion battery cathodes, inherently possess numerous advantages like good thermal stability, air stability, and structural stability. However, they also face fundamental challenges in applying the high-entropy strategy due to limitations such as their rigid polyanionic frameworks, low dopant compatibility, and redox mismatch. Furthermore, the performance gains from entropy-driven stability enhancement appear less pronounced. Nevertheless, it is worth noting that the application potential of the high-entropy strategy in this direction remains significant. Some researchers have successfully utilized high-entropy approaches to optimize ion migration paths and barriers, inhibit lattice strain, and enhance redox reaction kinetics in polyanionic compounds, thereby overcoming inherent bottlenecks like conductivity and specific capacity and opening new frontiers in performance [59, 161]. In summary, high-entropy cathode materials emerge as a critical pathway for next-generation sodium-ion batteries by breaking through traditional constraints in energy density, cycle life, and structural stability. Future research should prioritize entropy-functionalized design, comprehensive optimization, advanced characterization integration, and cross-scale theoretical modeling, incorporating AI tools and commercialization considerations. This will facilitate a transition from passive validation of material properties to active design and establish a comprehensive understanding of high-entropy mechanisms.

Conflicts of Interest

The authors declare no conflicts of interest.

Data Availability Statement

The data that support the findings of this study are available from the corresponding author upon reasonable request.

References

1. C. A. Hunter, M. M. Penev, E. P. Reznicek, J. Eichman, N. Rustagi, and S. F. Baldwin, "Techno-Economic Analysis of Long-Duration Energy Storage and Flexible Power Generation Technologies to Support High-Variable Renewable Energy Grids," *Joule* 5, no. 8 (2021): 2077–2101, https://doi.org/10.1016/j.joule.2021.06.018.

2. H. He, J.-H. Mai, K.-S. Hu, et al., "Recent Advances in Electrocatalysts for Efficient Hydrogen Evolution Reaction," *Rare Metals* 44, no. 4 (2025): 2208–2238, https://doi.org/10.1007/s12598-024-02649-1.

3. S. Lai, T. Huang, P. Liu, et al., "Progress and Prospects of Graphene-based Materials in Lithium Batteries," *Rare Metals* 43, no. 5 (2024): 1886–1905, https://doi.org/10.1007/s12598-023-02565-w.

4. P. Liu, Z.-H. Zhu, W. Zhang, et al., "Shearing-Force-Driven Delamination of Waste Residue Into Oxidatively Stable Mxene Composites for High-Performance Si Anode," *Rare Metals* 42, no. 7 (2023): 2226–2237, https://doi.org/10.1007/s12598-022-02182-z.

5. B. Ma, Y.-L. Zhang, and X.-H. Liu, "Concept of Hydrophobic Li$^+$-Solvated Structure for High Performances Lithium Metal Batteries," *Rare Metals* 42, no. 5 (2023): 1427–1430, https://doi.org/10.1007/s12598-022-02217-5.

6. F. Zhan, K.-S. Hu, J.-H. Mai, et al., "Recent Progress of Pt-Based Oxygen Reduction Reaction Catalysts for Proton Exchange Membrane Fuel Cells," *Rare Metals* 43, no. 6 (2024): 2444–2468, https://doi.org/10.1007/s12598-023-02586-5.

7. N. Liu, Y. Zhan, R. Tan, G. Zhao, and J. Song, "Unlocking Carbon Capture and Storage Potential: Policy Incentives, Economic Challenges, and Infrastructure Integration for CO2 Transport," *Chain* 2, no. 3 (2025): 211–226, https://doi.org/10.23919/CHAIN.2025.000015.

8. X. Liu, M. Ouyang, M. W. Orzech, et al., "In-situ Fabrication of Carbon-Metal Fabrics as Freestanding Electrodes for High-Performance Flexible Energy Storage Devices," *Energy Storage Materials* 30 (2020): 329–336, https://doi.org/10.1016/j.ensm.2020.04.001.

9. Y. Feng, R. Tan, Y. Zhao, et al., "Insight Into Fast Ion Migration Kinetics of a New Hybrid Single Li-ion Conductor Based on Aluminate Complexes for Solid-State Li-ion Batteries," *Nanoscale* 10, no. 13 (2018): 5975–5984, https://doi.org/10.1039/c8nr00573g.

10. G. Bao, X. Liu, B. Zou, et al., "Collaborative Framework of Transformer and LSTM for Enhanced State-of-Charge Estimation in Lithium-ion Batteries," *Energy* 322 (2025): 135548, https://doi.org/10.1016/j.energy.2025.135548.

11. X. Liu, K. Yang, B. Zou, et al., "Accurate Estimation of State of Health for Lithium-ion Batteries Based on Pyraformer and TimeGAN

Data Augmentation," *Journal of Power Sources* 640 (2025): 236722, https://doi.org/10.1016/j.jpowsour.2025.236722.

12. X. Yang, W. Kong, G. Du, et al., "Synthesis of a Yolk-Shell Nanostructured Silicon-Based Anode for High-Performance Li-Ion Batteries," *Batteries* 9, no. 9 (2023): 446, https://doi.org/10.3390/batteries9090446.

13. B. Zou, L. Zhang, X. Xue, et al., "A Review on the Fault and Defect Diagnosis of Lithium-ion Battery for Electric Vehicles," *Energies* 16, no. 14 (2023): 5507, https://doi.org/10.3390/en16145507.

14. G. Chen, R. Tan, C. Zeng, et al., "Developing Safe and High-Performance Lithium-ion Batteries: Strategies and Approaches," *Progress in Materials Science* 154 (2025): 101516, https://doi.org/10.1016/j.pmatsci.2025.101516.

15. H. Zhang, Y. Huang, Y. Wang, et al., "In-Situ Constructed Protective Bilayer Enabling Stable Cycling of $LiCoO_2$ Cathode at High-Voltage," *Energy Storage Materials* 62 (2023): 102951, https://doi.org/10.1016/j.ensm.2023.102951.

16. Z. Wang, R. Tan, H. Wang, et al., "A Metal–Organic-Framework-Based Electrolyte With Nanowetted Interfaces for High-Energy-Density Solid-State Lithium Battery," *Advanced Materials* 30, no. 2 (2018): 1704436, https://doi.org/10.1002/adma.201704436.

17. B. Zhang, R. Tan, L. Yang, et al., "Mechanisms and Properties of ion-Transport in Inorganic Solid Electrolytes," *Energy Storage Materials* 10 (2018): 139–159, https://doi.org/10.1016/j.ensm.2017.08.015.

18. X. Tian, C. Ye, L. Zhang, et al., "Enhancing Membrane Materials for Efficient Li Recycling and Recovery," *Advanced Materials* 37, no. 5 (2025): 2402335, https://doi.org/10.1002/adma.202402335.

19. W. Zheng, G. Liang, H. Guo, et al., "Enhancing the Reaction Kinetics and Structural Stability of High-Voltage $LiCoO_2$ via Polyanionic Species Anchoring," *Energy & Environmental Science* 17, no. 12 (2024): 4147–4156, https://doi.org/10.1039/d4ee00726c.

20. Y. Li, X. Liu, L. Wang, et al., "Thermal Runaway Mechanism of Lithium-ion Battery With $LiNi_{0.8}Mn_{0.1}Co_{0.1}O_2$ Cathode Materials," *Nano Energy* 85 (2021): 105878, https://doi.org/10.1016/j.nanoen.2021.105878.

21. Z. Li, Y. X. Yao, M. Zheng, et al., "Electrolyte Design Enables Rechargeable LiFePO4/Graphite Batteries From −80°C to 80°C," *Angewandte Chemie International Edition* 64, no. 2 (2024): e202409409, https://doi.org/10.1002/anie.202409409.

22. S. Peng, X. Yan, X. Wu, et al., "Thin Skinned Asymmetric Polybenzimidazole Membranes With Readily Tunable Morphologies for High-Performance Vanadium Flow Batteries," *RSC Advances* 7, no. 4 (2017): 1852–1862, https://doi.org/10.1039/c6ra24801b.

23. G. Ji, D. Tang, J. Wang, et al., "Sustainable Upcycling of Mixed Spent Cathodes to a High-Voltage Polyanionic Cathode Material," *Nature Communications* 15, no. 1 (2024): 4086, https://doi.org/10.1038/s41467-024-48181-9.

24. Z. Li, Y. Wang, J. Wang, et al., "Gradient-Porous-Structured Ni-Rich Layered Oxide Cathodes With High Specific Energy and Cycle Stability for Lithium-ion Batteries," *Nature Communications* 15, no. 1 (2024): 10216, https://doi.org/10.1038/s41467-024-54637-9.

25. Y. Huang, Y. Dong, Y. Yang, et al., "Integrated Rocksalt–Polyanion Cathodes With Excess Lithium and Stabilized Cycling," *Nature Energy* 9, no. 12 (2024): 1497–1505, https://doi.org/10.1038/s41560-024-01615-6.

26. P. Zou, L. Yao, C. Wang, S. J. Lee, T. Li, and H. L. Xin, "Regulating Cation Interactions for Zero-Strain and High-Voltage P2-type $Na_{2/3}Li_{1/6}Co_{1/6}Mn_{2/3}O_2$ Layered Oxide Cathodes of Sodium-Ion Batteries," *Angewandte Chemie International Edition* 62, no. 28 (2023): e202304628, https://doi.org/10.1002/anie.202304628.

27. H. Zhang, Y. Gao, J. Peng, et al., "Prussian Blue Analogues With Optimized Crystal Plane Orientation and Low Crystal Defects Toward 450 Wh kg−1 Alkali-Ion Batteries," *Angewandte Chemie International Edition* 62, no. 27 (2023): e202303953, https://doi.org/10.1002/anie.202303953.

28. Z. Zou, Y. Mu, M. Han, et al., "Integrated Polyanion-Layered Oxide Cathodes Enabling 100 000 Cycle Life for Sodium-ion Batteries," *Energy & Environmental Science* 18, no. 5 (2025): 2216–2230, https://doi.org/10.1039/d4ee05110f.

29. Y. Xiao, Q. Q. Sun, D. Chen, et al., "Guideline of Dynamic Tunnel Structural Evolution for Durable Sodium-Ion Oxide Cathodes," *Advanced Materials* 37, no. 30 (2025): 2504312, https://doi.org/10.1002/adma.202504312.

30. L. Deng, F.-D. Yu, Y. Xia, et al., "Stabilizing Fluorine to Achieve High-Voltage and Ultra-Stable $Na_3V_2(PO_4)_2F_3$ Cathode for Sodium Ion Batteries," *Nano Energy* 82 (2021): 105659, https://doi.org/10.1016/j.nanoen.2020.105659.

31. Y. Yao, M. Pei, C. Su, et al., "A Small-Molecule Organic Cathode With Extended Conjugation Toward Enhancing Na+ Migration Kinetics for Advanced Sodium-Ion Batteries," *Small* 20, no. 34 (2024): 2401481, https://doi.org/10.1002/smll.202401481.

32. L. Yang, Z. Wang, Y. Feng, et al., "Flexible Composite Solid Electrolyte Facilitating Highly Stable "Soft Contacting" Li–Electrolyte Interface for Solid State Lithium-Ion Batteries," *Advanced Energy Materials* 7, no. 22 (2017): 1701437, https://doi.org/10.1002/aenm.201701437.

33. C. Shi, Z. Li, M. Wang, et al., "Electrolyte Tailoring and Interfacial Engineering for Safe and High-Temperature Lithium-ion Batteries," *Energy & Environmental Science* 18, no. 7 (2025): 3248–3258, https://doi.org/10.1039/d4ee05263c.

34. C. Shi, M. Wang, Z. Tehrani, et al., "Constructing Quasi-Localized High-Concentration Solvation Structures to Stabilize Battery Interfaces in Nonflammable Phosphate-Based Electrolyte," *Advanced Science* 12, no. 6 (2025): 2411826, https://doi.org/10.1002/advs.202411826.

35. J. Lai, R. Tan, H. Jiang, et al., "Development of an in Situ Polymerized Artificial Layer for Dendrite-Free and Stable Lithium Metal Batteries," *Battery Energy* 3, no. 4 (2024): 20230070, https://doi.org/10.1002/bte2.20230070.

36. H. Hao, R. Tan, C. Ye, and C. T. J. Low, "Carbon-Coated Current Collectors in Lithium-Ion Batteries and Supercapacitors: Materials, Manufacture and Applications," *Carbon Energy* 6, no. 12 (2024): e604, https://doi.org/10.1002/cey2.604.

37. L. Li, J. Yang, R. Tan, et al., "Large-Scale Current Collectors for Regulating Heat Transfer and Enhancing Battery Safety," *Nature Chemical Engineering* 1, no. 8 (2024): 542–551, https://doi.org/10.1038/s44286-024-00103-8.

38. Y. Gan, M. Liu, R. Tan, et al., "Flame-Retardant Crosslinked Polymer Stabilizes Graphite–Silicon Composite Anode for Self-Extinguishing Lithium-Ion Batteries," *Advanced Energy Materials* 12, no. 45 (2022): 2202779, https://doi.org/10.1002/aenm.202202779.

39. X. Sun, M. Ouyang, and H. Hao, "Surging Lithium Price Will Not Impede the Electric Vehicle Boom," *Joule* 6, no. 8 (2022): 1738–1742, https://doi.org/10.1016/j.joule.2022.06.028.

40. R. Gao, R. Tan, L. Han, et al., "Nanofiber Networks of $Na_3V_2(PO_4)_3$ as a Cathode Material for High Performance All-Solid-State Sodium-ion Batteries," *Journal of Materials Chemistry A* 5, no. 11 (2017): 5273–5277, https://doi.org/10.1039/c7ta00314e.

41. R. Tan, A. Wang, R. Malpass-Evans, et al., "Hydrophilic Microporous Membranes for Selective Ion Separation and Flow-Battery Energy Storage," *Nature Materials* 19, no. 2 (2020): 195–202, https://doi.org/10.1038/s41563-019-0536-8.

42. Y. Yuan, J. Yang, Z. Liu, et al., "A Proton-Barrier Separator Induced via Hofmeister Effect for High-Performance Electrolytic MnO_2–Zn Batteries," *Advanced Energy Materials* 12, no. 16 (2022): 2103705, https://doi.org/10.1002/aenm.202103705.

43. C. Yin, X. Liu, J. Wei, et al., "'All-in-Gel' Design for Supercapacitors Towards Solid-State Energy Devices With Thermal and Mechanical Compliance," *Journal of Materials Chemistry A* 7, no. 15 (2019): 8826–8831, https://doi.org/10.1039/c9ta01155b.

44. A. Wang, C. Breakwell, F. Foglia, et al., "Selective Ion Transport Through Hydrated Micropores in Polymer Membranes," *Nature* 635, no. 8038 (2024): 1–6, https://doi.org/10.1038/s41586-024-08140-2.

45. J. M. Tuffnell, J. K. Morzy, N. D. Kelly, et al., "Comparison of the Ionic Conductivity Properties of Microporous and Mesoporous Mofs Infiltrated With a Na-ion Containing IL Mixture," *Dalton Transactions* 49, no. 44 (2020): 15914–15924, https://doi.org/10.1039/d0dt02576c.

46. R. Tan, H. He, A. Wang, et al., "Interfacial Engineering of Polymer Membranes With Intrinsic Microporosity for Dendrite-Free Zinc Metal Batteries," *Angewandte Chemie International Edition* 63, no. 49 (2024): e202409322, https://doi.org/10.1002/anie.202409322.

47. W. Zheng, G. M. Liang, Q. Liu, et al., "The Promise of High-Entropy Materials for High-Performance Rechargeable Li-ion and Na-ion Batteries," *Joule* 7, no. 12 (2023): 2732–2748, https://doi.org/10.1016/j.joule.2023.10.016.

48. Y. S. Zheng, Y. F. Meng, X. Hu, et al., "Synthesis-Structure-Property of High-Entropy Layered Oxide Cathode for Li/Na/K-Ion Batteries," *Advanced Materials* 37, no. 1 (2025): 2413202, https://doi.org/10.1002/adma.202413202.

49. T. Wenjie, T. Yongwei, L. Mengting, C. Yonghong, and W. Peng-Fei, "Layered Oxide Cathodes for Potassium-ion Batteries: Challenges, Strategies and Perspectives," *Energy Materials* 5, no. 11 (2025): 500140, https://doi.org/10.20517/energymater.2025.11.

50. S. Krouna, A. Acheche, G. Wang, et al., "Atomic-Scale Insights Into the Thermal Stability of High-Entropy Nanoalloys," *Advanced Materials* 37, no. 4 (2025): 2414510, https://doi.org/10.1002/adma.202414510.

51. M. Lian, W. Gong, S. Guo, Y. Jiang, and Z. Ye, "Unveiling the Potential of High-Entropy Materials Toward High-Energy Metal Batteries Based on Conversion Reactions: Synthesis, Structure, Properties, and Beyond," *Energy Storage Materials* 75 (2025): 104054, https://doi.org/10.1016/j.ensm.2025.104054.

52. V. Verma, C. H. Belcher, D. Apelian, E. J. Lavernia, C. H. Belcher, D. Apelian, and E. J. Lavernia, "Diffusion in High Entropy Alloy Systems—A Review," *Progress in Materials Science* 142 (2024): 101245, https://doi.org/10.1016/j.pmatsci.2024.101245.

53. Z. Zhou, Y. Ma, T. Brezesinski, B. Breitung, Y. Wu, and Y. Ma, "Improving Upon Rechargeable Battery Technologies: On the Role of High-Entropy Effects," *Energy & Environmental Science* 18, no. 1 (2025): 19–52, https://doi.org/10.1039/d4ee03708a.

54. J. W. Yeh, S. K. Chen, S. J. Lin, et al., "Nanostructured High-Entropy Alloys With Multiple Principal Elements: Novel Alloy Design Concepts and Outcomes," *Advanced Engineering Materials* 6, no. 5 (2004): 299–303, https://doi.org/10.1002/adem.200300567.

55. K. Wang, W. Hua, X. Huang, et al., "Synergy of Cations in High Entropy Oxide Lithium Ion Battery Anode," *Nature Communications* 14, no. 1 (2023): 1487, https://doi.org/10.1038/s41467-023-37034-6.

56. W.-L. Hsu, C.-W. Tsai, A.-C. Yeh, and J.-W. Yeh, "Clarifying the Four Core Effects of High-Entropy Materials," *Nature Reviews Chemistry* 8, no. 6 (2024): 471–485, https://doi.org/10.1038/s41570-024-00602-5.

57. X. Chen, K. Chen, F. Ji, et al., "Achieving Fast Ion/Electron Transportation and Smooth Phase Transition in Polyanion Cathode by the High Entropy Strategy," *Advanced Energy Materials* 15, no. 26 (2025): 2500502, https://doi.org/10.1002/aenm.202500502.

58. P. Dong, F. Peng, Q. Zhang, et al., "High Entropy Boosts the Low Temperature Na^+-Storage Performance of $Na_4Fe_3(PO_4)_2P_2O_7$," *Angewandte Chemie-International Edition* 64, no. 21 (2025): e202502693, https://doi.org/10.1002/anie.202502693.

59. M. Du, K. Li, N. Yu, et al., "Ultrafast Preparation of High-Entropy NASICON Cathode Enables Stabilized Multielectron Redox and Wide-Temperature (-50–$60°C$) Workability in Sodium-Ion Batteries," *Advanced Materials* 37, no. 9 (2025): 2418219, https://doi.org/10.1002/adma.202418219.

60. T. Sheng, L. Wang, H. Nie, et al., "Modulating Phase Angle Variations of O3-Type High-Entropy Layered Sodium Oxide for Practical Sodium-Ion Cylindrical Battery," *Advanced Functional Materials* 35, no. 34 (2025): 2501688, https://doi.org/10.1002/adfm.202501688.

61. Y. Ma, Y. Ma, S. L. Dreyer, et al., "High-Entropy Metal-Organic Frameworks for Highly Reversible Sodium Storage," *Advanced Materials* 33, no. 34 (2021): 2101342, https://doi.org/10.1002/adma.202101342.

62. X. Chen, L. Han, Y. Zhao, Y. Cao, and Y. Fang, "Insights in Iron-based Polyanion Electrode Materials for Advanced Sodium-ion Batteries," *Chemical Engineering Journal* 501 (2024): 157600, https://doi.org/10.1016/j.cej.2024.157600.

63. Y. Dong, Z. Zhou, Y. Ma, et al., "Layered-Structured Sodium-Ion Cathode Materials: Advancements Through High-Entropy Approaches," *ACS Energy Letters* 9, no. 10 (2024): 5096–5119, https://doi.org/10.1021/acsenergylett.4c02223.

64. L. Wang, L. Wang, H. Wang, et al., "Progress and Perspective of High-Entropy Strategy Applied in Layered Transition Metal Oxide Cathode Materials for High-Energy and Long Cycle Life Sodium-Ion Batteries," *Advanced Functional Materials* 35, no. 11 (2025): 2417258, https://doi.org/10.1002/adfm.202417258.

65. T. Yang, X. Wang, Z. Liu, and Q. Liu, "Cation Configuration and Structural Degradation of Layered Transition Metal Oxides in Sodium-Ion Batteries," *ACS Nano* 18, no. 29 (2024): 18834–18851, https://doi.org/10.1021/acsnano.4c05739.

66. X. Cai, Z. Shadike, N. Wang, et al., "Constraining Interlayer Slipping in P2-Type Layered Oxides With Oxygen Redox by Constructing Strong Covalent Bonds," *Journal of the American Chemical Society* 147, no. 7 (2025): 5860–5870, https://doi.org/10.1021/jacs.4c14587.

67. H. Wang, X. Gao, S. Zhang, et al., "High-Entropy Na-Deficient Layered Oxides for Sodium-Ion Batteries," *ACS Nano* 17, no. 13 (2023): 12530–12543, https://doi.org/10.1021/acsnano.3c02290.

68. Y. Sun, J. Ma, D. Wu, et al., "A Breathable Inorganic-Organic Interface for Fabricating a Crack-Free Nickel-Rich Cathode With Long-Term Stability," *Energy & Environmental Science* 17, no. 14 (2024): 5124–5136, https://doi.org/10.1039/d4ee01254b.

69. Y. Yang, Z. Wang, C. Du, et al., "Decoupling the Air Sensitivity of Na-layered Oxides," *Science* 385, no. 6710 (2024): 744–752, https://doi.org/10.1126/science.adm9223.

70. H. Li, J. Wang, S. Xu, et al., "Universal Design Strategy for Air-Stable Layered Na-Ion Cathodes Toward Sustainable Energy Storage," *Advanced Materials* 36, no. 27 (2024): 2403073, https://doi.org/10.1002/adma.202403073.

71. W. Zhang, C. Yuan, J. Zhu, T. Jin, C. Shen, and K. Xie, "Air Instability of Ni-Rich Layered Oxides-A Roadblock to Large Scale Application," *Advanced Energy Materials* 13, no. 2 (2023): 2202993, https://doi.org/10.1002/aenm.202202993.

72. C. Jiang, B. Chen, M. Xu, and J. Jiang, "Elevating Both Capacity and Voltage Tolerance of P2-Type Layered Cathodes With Cooperative Al Cation/F Anion co-Doping for Advanced Sodium-ion Batteries," *Energy Storage Materials* 70 (2024): 103518, https://doi.org/10.1016/j.ensm.2024.103518.

73. J. Zhang, Z. Yu, Y. Zhu, et al., "Configuration Design and Interface Reconstruction to Realize the Superior High-Rate Performance for Sodium Layered Oxide Cathodes," *Advanced Energy Materials* 15, no. 23 (2025): 2405951, https://doi.org/10.1002/aenm.202405951.

74. X. Cai, P. Yan, T. Xie, et al., "Pinning the Surface Layered Oxide Structure in High Temperature Calcination Using Conformal Atomic

Layer Deposition Coating for Fast Charging Cathode," *Advanced Functional Materials* 35, no. 17 (2025): 2423888, https://doi.org/10.1002/adfm.202423888.

75. C. Cheng, Z. Zhuo, X. Xia, et al., "Stabilized Oxygen Vacancy Chemistry Toward High-Performance Layered Oxide Cathodes for Sodium-Ion Batteries," *ACS Nano* 18, no. 51 (2024): 35052–35065, https://doi.org/10.1021/acsnano.4c14724.

76. Z. Liu, R. Liu, S. Xu, et al., "Achieving a Deeply Desodiated Stabilized Cathode Material by the High Entropy Strategy for Sodium-ion Batteries," *Angewandte Chemie-International Edition* 63, no. 29 (2024): e202405620, https://doi.org/10.1002/anie.202405620.

77. X. Wang, Q. Kang, J. Sun, et al., "High-Entropy Engineering Enables O3-Type Layered Oxide With High Structural Stability and Reaction Kinetic for Sodium Storage," *Journal of Colloid and Interface Science* 691 (2025): 137438, https://doi.org/10.1016/j.jcis.2025.137438.

78. R. Ma, J. Wang, G. Zhu, et al., "Multicomponent High-Entropy Assisted High-Rate and Air-Stable Layered Cathode for Sodium Ion Batteries," *Green Energy & Environment* 10, no. 8 (2025): 1797–1806, https://doi.org/10.1016/j.gee.2025.03.008.

79. L.-T. Lv, Z.-J. Zhu, M.-Y. Shen, T. Wu, B. He, and W.-C. Li, "Cu and Fe Doping Realized a High Rate and Low Volume Strain O3-Type Layered Oxide Cathode for Sodium Ion Batteries," *Journal of Materials Chemistry A* 13, no. 21 (2025): 16122–16131, https://doi.org/10.1039/d5ta01954k.

80. B. Ouyang and Y. Zeng, "The Rise of High-Entropy Battery Materials," *Nature Communications* 15, no. 1 (2024): 973, https://doi.org/10.1038/s41467-024-45309-9.

81. B. Wang, J. Ma, K. Wang, et al., "High-Entropy Phase Stabilization Engineering Enables High-Performance Layered Cathode for Sodium-Ion Batteries," *Advanced Energy Materials* 14, no. 23 (2024): 2401090, https://doi.org/10.1002/aenm.202401090.

82. X. Z. Wang, Y. Zuo, Y. Qin, et al., "Fast Na+ Kinetics and Suppressed Voltage Hysteresis Enabled by a High-Entropy Strategy for Sodium Oxide Cathodes," *Advanced Materials* 36, no. 24 (2024): 2312300, https://doi.org/10.1002/adma.202312300.

83. W. Dong, L. Wu, B. Liu, et al., "Fast-Charging High-Entropy O3-Type Layered Cathodes for Sodium-ion Batteries," *Chemical Engineering Journal* 504 (2025): 158997, https://doi.org/10.1016/j.cej.2024.158997.

84. Y. Dang, Z. Xu, Y. Wu, et al., "Boron-Doped High-Entropy Oxide Toward High-Rate and Long-Cycle Layered Cathodes for Wide-Temperature Sodium-ion Batteries," *Journal of Energy Chemistry* 95 (2024): 577–587, https://doi.org/10.1016/j.jechem.2024.03.055.

85. R. Li, X. Qin, X. Li, et al., "High-Entropy and Multiphase Cathode Materials for Sodium-Ion Batteries," *Advanced Energy Materials* 14, no. 26 (2024): 2400127, https://doi.org/10.1002/aenm.202400127.

86. J. Kuang, Z. Liu, L. Fu, et al., "Charge Tuning and Anchor Effect Achieving Stable High-Voltage Layered Metal Oxides for Sodium-Ion Battery," *Angewandte Chemie-International Edition* 64, no. 21 (2025): e202500715, https://doi.org/10.1002/anie.202500715.

87. T. Zhang, Y. Li, Z. Song, et al., "Insights Into Chemical-Mechanical Degradation and Modification Strategies of Layered Oxide Cathode Materials of Sodium Ion Batteries," *Journal of Energy Chemistry* 103 (2025): 294–315, https://doi.org/10.1016/j.jechem.2024.11.068.

88. F. Ding, P. Ji, Z. Han, et al., "Tailoring Planar Strain for Robust Structural Stability in High-Entropy Layered Sodium Oxide Cathode Materials," *Nature Energy* 9, no. 12 (2024): 1529–1539, https://doi.org/10.1038/s41560-024-01616-5.

89. T. Cai, M. Cai, J. Mu, et al., "High-Entropy Layered Oxide Cathode Enabling High-Rate for Solid-State Sodium-Ion Batteries," *Nano-Micro Letters* 16, no. 1 (2024): 10, https://doi.org/10.1007/s40820-023-01232-0.

90. H. Wang, J. Gao, Y. Mei, et al., "Halting Oxygen Evolution to Achieve Long Cycle Life in Sodium Layered Cathodes," *Angewandte Chemie-International Edition* 64, no. 6 (2025): e202418605, https://doi.org/10.1002/anie.202418605.

91. L. Yao, P. Zou, C. Wang, et al., "High-Entropy and Superstructure-Stabilized Layered Oxide Cathodes for Sodium-Ion Batteries," *Advanced Energy Materials* 12, no. 41 (2022): 2201989, https://doi.org/10.1002/aenm.202201989.

92. S. Liu, F. Liu, S. Zhao, et al., "A High-Entropy Engineering on Sustainable Anionic Redox Mn-Based Cathode With Retardant Stress for High-Rate Sodium-Ion Batteries," *Angewandte Chemie-International Edition* 64, no. 10 (2025): e202421089, https://doi.org/10.1002/anie.202421089.

93. L. Liu, Y. Xin, Y. Wang, et al., "High-Entropy Configuration of O3-Type Layered Transition-Metal Oxide Cathode With High-Voltage Stability for Sodium-ion Batteries," *Journal of Materials Chemistry A* 12, no. 35 (2024): 23495–23505, https://doi.org/10.1039/d4ta04371e.

94. Z. Huang, S. Wang, X. Guo, et al., "High-Entropy Layered Oxide Cathode Materials With Moderated Interlayer Spacing and Enhanced Kinetics for Sodium-Ion Batteries," *Advanced Materials* 36, no. 50 (2024): 2410857, https://doi.org/10.1002/adma.202410857.

95. X. Gui, Z. Xiang, T. Ren, et al., "High-Entropy Doped P′2 Mn-Based Layered Oxide With Superior Stability and High Capacity for Sodium-Ion Batteries," *Advanced Materials* 37, no. 20 (2025): 2417008, https://doi.org/10.1002/adma.202417008.

96. J. Zhan, J. Huang, Z. Li, et al., "Air-Stable High-Entropy Layered Oxide Cathode With Enhanced Cycling Stability for Sodium-Ion Batteries," *Nano Letters* 24, no. 32 (2024): 9793–9800, https://doi.org/10.1021/acs.nanolett.4c00968.

97. X.-Q. Xu, J.-Y. Chen, Y. Jiang, et al., "Origins of High Air Sensitivity and Treatment Strategies in O3-Type $NaMn_{1/3}Fe_{1/3}Ni_{1/3}O_2$," *Journal of the American Chemical Society* 146, no. 32 (2024): 22374–22386, https://doi.org/10.1021/jacs.4c05255.

98. L.-Y. Kong, J.-Y. Li, H.-X. Liu, et al., "A Universal Interfacial Reconstruction Strategy Based on Converting Residual Alkali for Sodium Layered Oxide Cathodes: Marvelous Air Stability, Reversible Anion Redox, and Practical Full Cell," *Journal of the American Chemical Society* 146, no. 47 (2024): 32317–32332, https://doi.org/10.1021/jacs.4c04766.

99. S. Jia, S. Kumakura, and E. McCalla, "Unravelling Air/Moisture Stability of Cathode Materials in Sodium Ion Batteries: Characterization, Rational Design, and Perspectives," *Energy & Environmental Science* 17, no. 13 (2024): 4343–4389, https://doi.org/10.1039/D4EE00796D.

100. L. Huang, J. Zhu, J.-X. Liu, H. Wu, and G.-J. Zhang, "High Entropy Stabilized O3-Type $NaNi_{0.3}Fe_{0.2}Mn_{0.2}Ti_{0.15}Sn_{0.15}O_2$ Cathode Material for Sodium-ion Batteries," *Chemical Engineering Journal* 507 (2025): 160309, https://doi.org/10.1016/j.cej.2025.160309.

101. A. Joshi, S. Chakrabarty, S. H. Akella, et al., "High-Entropy Co-Free O3-Type Layered Oxyfluoride: A Promising Air-Stable Cathode for Sodium-Ion Batteries," *Advanced Materials* 35, no. 51 (2023): 2304440, https://doi.org/10.1002/adma.202304440.

102. J. Qiu, M. Qin, F. Huang, et al., "High-Entropy Configuration Regulating Interlayer Oxygen Charge Toward High-Voltage and Air-Stability Layered Cathode in High-Loading Sodium Ion Full Batteries," *Advanced Functional Materials* 35, no. 29 (2025): 2500158, https://doi.org/10.1002/adfm.202500158.

103. K. Tian, Y. Dang, Z. Xu, et al., "A Three-in-One Strategy of High-Entropy, Single-Crystal, and Biphasic Approaches to Design O3-Type Layered Cathodes for Sodium-ion Batteries," *Energy Storage Materials* 73 (2024): 103841, https://doi.org/10.1016/j.ensm.2024.103841.

104. K. Zhang, Y. Niu, H. Xing, et al., "Revealing the Self-Regulating Phase Transition Mechanism of Low-Volume P2+"Z" in P2-Type Sodium Manganese With High-Entropy Substitution for Sodium-Ion Batteries," *Small* 21, no. 21 (2025): 2407524, https://doi.org/10.1002/smll.202407524.

105. A. Ghosh, R. Hegde, and P. Senguttuvan, "A High Entropy O3-$Na_{1.0}Li_{0.1}Ni_{0.3}Fe_{0.1}Mn_{0.25}Ti_{0.25}O_2$ Cathode With Reversible Phase Transitions and Superior Electrochemical Performances for Sodium-ion Batteries," *Journal of Materials Chemistry A* 12, no. 24 (2024): 14583–14594, https://doi.org/10.1039/d4ta01137f.

106. H. Wang, T. Liu, H. Chen, et al., "Multicationic Interactions Mitigating Lattice Strain in Sodium Layered Cathodes," *Nature Communications* 16, no. 1 (2025): 4409, https://doi.org/10.1038/s41467-025-59666-6.

107. J. Yue, F. Xiong, Z. Shadike, et al., "A Layer-Structured High Entropy Oxide With Highly Reversible Fe3+/Fe4+ Redox as Advanced Cathode Material for Sodium Ion Batteries," *Journal of Power Sources* 627 (2025): 235735, https://doi.org/10.1016/j.jpowsour.2024.235735.

108. W. Qiu, Z. Chen, Z. Liu, et al., "Rational Design of High-Entropy Cathodes to Optimize Fast Charging Performance in Sodium-Ion Batteries," *Advanced Functional Materials* 35, no. 36 (2025): 2422106, https://doi.org/10.1002/adfm.202422106.

109. H. Chen, Z. Wang, Y. Shi, et al., "High-Entropy Modulation on Na-O Configuration Toward Ultrastable Sodium Layered Oxide," *Small* 21, no. 26 (2025): 2501933, https://doi.org/10.1002/smll.202501933.

110. L. Feng, Y. Xia, J. Guo, et al., "La-Doped O3-Type Layered Oxide Cathode With Enhanced Cycle Stability for Sodium-ion Batteries," *Chemical Engineering Journal* 496 (2024): 154298, https://doi.org/10.1016/j.cej.2024.154298.

111. M. Liu, Z.-K. Guan, X.-Z. Wang, et al., "High-Voltage Phase Stabilization and Air-Stability Enhancement in O3-Type Entropy-Reinforced Sodium Layered Cathodes," *Nano Energy* 142 (2025): 111216, https://doi.org/10.1016/j.nanoen.2025.111216.

112. L. Zhao, S. Bi, J. Li, et al., "Prussian Blue Analogues for Advanced Non-Aqueous Sodium Ion Batteries: Redox Mechanisms, Key Challenges and Modification Strategies," *Energy Storage Materials* 78 (2025): 104256, https://doi.org/10.1016/j.ensm.2025.104256.

113. X. Liu, Y. Cao, and J. Sun, "Defect Engineering in Prussian Blue Analogs for High-Performance Sodium-Ion Batteries," *Advanced Energy Materials* 12, no. 46 (2022): 2202532, https://doi.org/10.1002/aenm.202202532.

114. H. Zhang, J. Li, J. Liu, et al., "Understanding Capacity Fading From Structural Degradation in Prussian Blue Analogues for Wide-Temperature Sodium-ion Cylindrical Battery," *Nature Communications* 16, no. 1 (2025): 2520, https://doi.org/10.1038/s41467-025-57663-3.

115. J. Liu, J. Liu, M. Tang, J. Fu, X. Kuang, and J. Ma, "Boosting Sodium Storage in Prussian Blue Analogs Through Iron Vacancies and Copper Doping," *Advanced Functional Materials* 34, no. 17 (2024): 2314167, https://doi.org/10.1002/adfm.202314167.

116. D. Yang, H. Wang, Y. Zhao, et al., "Achieving Ultra-Fast and Stable Sodium-Ion Batteries Through Deep Activation of Low-Spin Iron in Prussian Blue," *Advanced Functional Materials* 35, no. 34 (2025): 2503067, https://doi.org/10.1002/adfm.202503067.

117. M. Wan, R. Zeng, J. Meng, et al., "Post-Synthetic and in Situ Vacancy Repairing of Iron Hexacyanoferrate Toward Highly Stable Cathodes for Sodium-Ion Batteries," *Nano-Micro Letters* 14, no. 1 (2022): 9, https://doi.org/10.1007/s40820-021-00742-z.

118. L. Ge, Y. Song, P. Niu, et al., "Elaborating the Crystal Water of Prussian Blue for Outstanding Performance of Sodium Ion Batteries," *ACS Nano* 18, no. 4 (2024): 3542–3552, https://doi.org/10.1021/acsnano.3c11169.

119. W. Wang, Y. Gang, J. Peng, et al., "Effect of Eliminating Water in Prussian Blue Cathode for Sodium-Ion Batteries," *Advanced Functional Materials* 32, no. 25 (2022): 2111727, https://doi.org/10.1002/adfm.202111727.

120. J. Li, L. Liu, Y. Gao, et al., "Ion-Exchange Synthesis of Low-Water Prussian Blue Analogs for Enhanced Sodium Storage," *Ecomat* 7, no. 2 (2025): e70000, https://doi.org/10.1002/eom2.70000.

121. E. Pastor, M. Sachs, S. Selim, J. R. Durrant, A. A. Bakulin, and A. Walsh, "Electronic Defects in Metal Oxide Photocatalysts," *Nature Reviews Materials* 7, no. 7 (2022): 503–521, https://doi.org/10.1038/s41578-022-00433-0.

122. Z. Wang, M. T. Sougrati, Y. He, et al., "Sodium Storage and Capacity Retention Behavior Derived From High-Spin/Low-Spin Fe Redox Reaction in Monoclinic Prussian Blue Based on Operando Mossbauer Characterization," *Nano Energy* 109 (2023): 108256, https://doi.org/10.1016/j.nanoen.2023.108256.

123. Z. Su, Z. Li, X. Yang, X. Li, L. Wang, and W. Lu, "In Situ Balanced Synthesis of High-Activity Low-Spin Iron Cathode Prussian Blue for Enhanced Sodium-Ion Storage," *Nano Letters* 25, no. 3 (2025): 957–965, https://doi.org/10.1021/acs.nanolett.4c03985.

124. B. Yuan, S. Qiao, L. Yuan, B. Chen, and S. Chong, "Zero-Strain Sodium Nickel Ferrocyanide as Cathode Material for Sodium-Ion Batteries With Ultra-Long Lifespan," *Small* 21, no. 1 (2025): 2407570, https://doi.org/10.1002/smll.202407570.

125. Z. Jing, L. Kong, M. Mamoor, et al., "Rational Design of Prussian Blue Analogues for Ultralong and Wide-Temperature-Range Sodium-Ion Batteries," *Journal of the American Chemical Society* 147, no. 4 (2025): 3702–3713, https://doi.org/10.1021/jacs.4c16031.

126. X. Gao, L. Guo, S. Zhang, et al., "Unveiling the Influence of Cyanogen Vacancies in Prussian Blue for Sodium-ion Batteries," *Angewandte Chemie International Edition* 64, (2025): e202421916, https://doi.org/10.1002/anie.202421916.

127. J. Dai, S. Tan, L. Wang, et al., "High-Voltage Potassium Hexacyanoferrate Cathode via High-Entropy and Potassium Incorporation for Stable Sodium-Ion Batteries," *ACS Nano* 17, no. 21 (2023): 20949–20961, https://doi.org/10.1021/acsnano.3c02323.

128. X. Zhao, Z. Xing, and C. Huang, "Investigation of High-Entropy Prussian Blue Analog as Cathode Material for Aqueous Sodium-ion Batteries," *Journal of Materials Chemistry A* 11, no. 42 (2023): 22835–22844, https://doi.org/10.1039/d3ta04349e.

129. Y. Huang, X. Zhang, L. Ji, et al., "Boosting the Sodium Storage Performance of Prussian Blue Analogs by Single-Crystal and High-Entropy Approach," *Energy Storage Materials* 58 (2023): 1–8, https://doi.org/10.1016/j.ensm.2023.03.011.

130. Y. Zhang, J. Huang, L. Qiu, et al., "Hollow Stair-Stepping Spherical High-Entropy Prussian Blue Analogue for High-Rate Sodium Ion Batteries," *ACS Applied Materials and Interfaces* 16, no. 21 (2024): 27684–27693, https://doi.org/10.1021/acsami.4c04785.

131. P. Dai, J. Huang, X. Cao, et al., "Central Metal Coordination Environment Optimization Enhances Na Diffusion and Structural Stability in Prussian Blue Analogues," *Energy Storage Materials* 74 (2025): 103890, https://doi.org/10.1016/j.ensm.2024.103890.

132. Y. Ma, Y. Hu, Y. Pramudya, et al., "Resolving the Role of Configurational Entropy in Improving Cycling Performance of Multicomponent Hexacyanoferrate Cathodes for Sodium-Ion Batteries," *Advanced Functional Materials* 32, no. 34 (2022): 2202372, https://doi.org/10.1002/adfm.202202372.

133. J. Peng, B. Zhang, W. Hua, et al., "A Disordered Rubik's Cube-Inspired Framework for Sodium-Ion Batteries With Ultralong Cycle Lifespan," *Angewandte Chemie-International Edition* 62, no. 6 (2023): e202215865, https://doi.org/10.1002/anie.202215865.

134. Y. He, S. L. Dreyer, Y.-Y. Ting, et al., "Entropy-Mediated Stable Structural Evolution of Prussian White Cathodes for Long-Life Na-Ion Batteries," *Angewandte Chemie-International Edition* 63, no. 7 (2024): e202315371, https://doi.org/10.1002/anie.202315371.

135. Z.-C. Jian, J.-X. Guo, Y.-F. Liu, Y.-F. Zhu, J. Wang, and Y. Xiao, "Cation Migration in Layered Oxide Cathodes for Sodium-ion Batteries: Fundamental Failure Mechanisms and Practical Modulation Strategies," *Chemical Science* 15, no. 47 (2024): 19698–19728, https://doi.org/10.1039/d4sc05206d.

136. N. Kar and S. E. Skrabalak, "Synthetic Methods for High-Entropy Nanomaterials," *Nature Reviews Materials* 10, no. 9 (2025): 638–653, https://doi.org/10.1038/s41578-025-00829-8.

137. Y. Ma, H. Du, S. Zheng, et al., "High-Entropy Approach vs. Traditional Doping Strategy for Layered Oxide Cathodes in Alkali-Metal-ion Batteries: A Comparative Study," *Energy Storage Materials* 79 (2025): 104295, https://doi.org/10.1016/j.ensm.2025.104295.

138. Q. Liu, Q. Du, X. Zhang, et al., "Characterization of Local Chemical Ordering and Deformation Behavior in High Entropy Alloys by Transmission Electron Microscopy," *International Journal of Minerals, Metallurgy and Materials* 31, no. 5 (2024): 877–886, https://doi.org/10.1007/s12613-024-2884-x.

139. X. Zhu, S.-W. Xu, X.-Z. Wang, M. Liu, Y. Cheng, and P.-F. Wang, "Sodium Composite Oxide Cathode Materials:Phase Regulation, Electrochemical Performance and Reaction Mechanism," *Batteries & Supercaps* 6, no. 3 (2023): e202200473, https://doi.org/10.1002/batt.202200473.

140. V. Sorkin, Z. G. Yu, S. Chen, T. L. Tan, Z. Aitken, and Y.-W. Zhang, "First Principles-Based Design of Lightweight High Entropy Alloys," *Scientific Reports* 13, no. 1 (2023): 22549, https://doi.org/10.1038/s41598-023-49258-z.

141. X. Wang, Q. Liu, and X. Wang, "High-Entropy Materials: From Bulk to Sub-Nano," *Advanced Functional Materials* 35, no. 32 (2025): 2504275, https://doi.org/10.1002/adfm.202504275.

142. L. Huang, J. Zhu, J.-X. Liu, H. Wu, and G.-J. Zhang, "Emerging High-Entropy Strategy: A Booster to the Development of Cathode Materials for Power Batteries," *Journal of Advanced Ceramics* 13, no. 8 (2024): 1093–1118, https://doi.org/10.26599/jac.2024.9220913.

143. J. Zander, J. P. Woelfel, M. Weiss, et al., "Medium- and High-Entropy Spinel Ferrite Nanoparticles via Low-Temperature Synthesis for the Oxygen Evolution Reaction," *Advanced Functional Materials* 34, no. 4 (2024): 2310179, https://doi.org/10.1002/adfm.202310179.

144. M. Du, J. Du, H. Fu, et al., "Quasi-Industrial Preparation of SWCNTs-Confined High-Entropy Oxides as Self-Supported Electrodes for Continuous Electrosynthesis," *Angewandte Chemie-International Edition* 64, no. 21 (2025): e202501669, https://doi.org/10.1002/anie.202501669.

145. G. He, X. Zhang, J. Liu, J. Chong, G. Ye, and H. Fei, "Hydro-carbothermal Flow Synthesis of Carbon-Supported Small and Dense High-Entropy Alloy Nanoparticles as Electrocatalysts," *Nature Communications* 16, no. 1 (2025): 8172, https://doi.org/10.1038/s41467-025-63527-7.

146. W. Yang, T. Xu, C. Yang, et al., "Selective and Bifunctional Catalytic Electrochemical Conversion of Organosulfide Molecule by High-Entropy Carbides," *Advanced Functional Materials* 34, no. 49 (2024): 2409450, https://doi.org/10.1002/adfm.202409450.

147. L. Duan, Y. Zhang, H. Tang, J. Liao, G. Zhou, and X. Zhou, "Recent Advances in High-Entropy Layered Oxide Cathode Materials for Alkali Metal-Ion Batteries," *Advanced Materials* 37, no. 1 (2025): 2411426, https://doi.org/10.1002/adma.202411426.

148. H. Gao, J. Li, F. Zhang, et al., "Revealing the Potential and Challenges of High-Entropy Layered Cathodes for Sodium-Based Energy Storage," *Advanced Energy Materials* 14, no. 20 (2024): 2304529, https://doi.org/10.1002/aenm.202304529.

149. S. Ma, P. Zou, and H. L. Xin, "Extending Phase-Variation Voltage Zones in P2-type Sodium Cathodes Through High-Entropy Doping for Enhanced Cycling Stability and Rate Capability," *Materials Today Energy* 38 (2023): 101446, https://doi.org/10.1016/j.mtener.2023.101446.

150. S. Nie, Y. Xiang, L. Wu, et al., "Active Learning Guided Discovery of High Entropy Oxides Featuring High H_2-Production," *Journal of the American Chemical Society* 146, no. 43 (2024): 29325–29334, https://doi.org/10.1021/jacs.4c06272.

151. M. H. Golbabaei, M. Zohrevand, and N. Zhang, "Applications of Machine Learning in High-Entropy Alloys: A Review of Recent Advances in Design, Discovery, and Characterization," *Nanoscale* 17, no. 36 (2025): 20548–20605, https://doi.org/10.1039/D5NR01562F.

152. S. Liu, B. Bocklund, J. Diffenderfer, et al., "A Comparative Study of Predicting High Entropy Alloy Phase Fractions With Traditional Machine Learning and Deep Neural Networks," *Npj Computational Materials* 10, no. 1 (2024): 172, https://doi.org/10.1038/s41524-024-01335-1.

153. J. Wang, H. Kwon, H. S. Kim, and B.-J. Lee, "A Neural Network Model for High Entropy Alloy Design," *Npj Computational Materials* 9, no. 1 (2023): 60, https://doi.org/10.1038/s41524-023-01010-x.

154. D. J. Sprouster, J. R. Trelewicz, L. L. Snead, et al., "Advanced Synchrotron Characterization Techniques for Fusion Materials Science," *Journal of Nuclear Materials* 543 (2021): 152574, https://doi.org/10.1016/j.jnucmat.2020.152574.

155. A. Ghose, M. Segal, F. Meng, et al., "Uncertainty-Aware Predictions of Molecular x-ray Absorption Spectra Using Neural Network Ensembles," *Physical Review Research* 5, no. 1 (2023): 013180, https://doi.org/10.1103/PhysRevResearch.5.013180.

156. X. Tian, S. Zhou, H. Hao, et al., "Machine Learning and Density Functional Theory for Catalyst and Process Design in Hydrogen Production," *Chain* 1, no. 2 (2024): 150–166, https://doi.org/10.23919/chain.2024.100004.

157. Z. Feng, I. Eiubovi, Y. Shao, Z. Fan, and R. Tan, "Review of Digital Twin Technology Applications in Hydrogen Energy," *Chain* 1, no. 1 (2024): 54–74, https://doi.org/10.23919/chain.2024.000001.

158. Z. Feng, Y. Luo, D. Li, J. Pan, R. Tan, and Y. Chen, "Integrating Digital Twins and Machine Learning for Advanced Control in Green Hydrogen Production," *Chain* 2, no. 1 (2025): 1–14, https://doi.org/10.23919/chain.2025.000003.

159. X. Liu, K. Yang, L. Zhang, et al., "A Fast Forward Prediction Framework for Energy Materials Design Based on Machine Learning Methods," *Energy Material Advances* 5 (2024): 0131, https://doi.org/10.34133/energymatadv.0131.

160. W. Zhang, L. He, J. Li, et al., "Configurational Entropy-Tailored NASICON Cathode Redox Chemistry for Capacity-Dense and Ultra-long Cyclability," *Energy & Environmental Science* 18, no. 14 (2025): 7278–7290, https://doi.org/10.1039/D5EE00877H.

161. H. Wang, Z. Zhang, Y. Chu, et al., "Boosting Na^+ Storage and Thermal Stability of $Na_4Fe_3(PO_4)_2P_2O_7$ via High-Entropy Engineering," *ACS Nano* 19, no. 49 (2025): 41824–41835, https://doi.org/10.1021/acsnano.5c15785.